Sensors & Actuators: B. Chemical 472 (2027) 141027

Contents lists available at ScienceDirect

Sensors and Actuators: B. Chemical

journal homepage: www.elsevier.com/locate/snb

Profiling the glycocalyx-shear stress interplay via high-throughput rotational single-cell optical biosensing

Igor Sallai [a,b,1], Dános Sebestyén Varga [a,c,1], Benjamin Csippa [d], Bálint Béres [a,e], Zoltán Szittner [a], Inna Székács [a], András Dér [c], Attila Bonyár [b,*], Robert Horvath [a,c,**]

[a] Nanobiosensorics Laboratory, Institute of Technical Physics and Materials Science, Centre for Energy Research, HUN-REN, Budapest, Hungary
[b] Department of Electronics Technology, Faculty of Electrical Engineering and Informatics, Budapest University of Technology and Economics, Budapest, Hungary
[c] Institute of Biophysics, HUN-REN Biological Research Centre, Szeged, Hungary
[d] Department of Hydrodynamic Systems, Budapest University of Technology and Economics, Budapest, Hungary
[e] Department of Automation and Applied Informatics, Faculty of Electrical Engineering and Informatics, Budapest University of Technology and Economics, Műegyetem rkp. 3, Budapest, H-1111, Hungary

ARTICLE INFO

Keywords:
Rotational fluidic system
Resonant waveguide grating
Biosensor
Single-cell
Glycocalyx
Computational fluid dynamics

ABSTRACT

Cells in living organisms are constantly exposed to fluid flow, which fundamentally influences their adhesion behavior and mechanobiological properties. Despite the critical role of flow in physiological and pathological processes, there are only a few experimental platforms that enable label-free investigation of flow-induced adhesion responses in large populations of individual cells under well-defined and tunable fluidic conditions. Here, we present a prototype device that integrates a resonant waveguide grating–based label-free optical biosensing approach with a custom-designed plate holder capable of inducing controlled rotation of the supernatant within standard well formats. This configuration allows real-time, single-cell–resolved monitoring of adhesion kinetics while dynamically modulating the mechanical environment experienced by the cells. We systematically examined the effects of fluidic field rotation across a range of rotation frequencies, as well as the impact of partial enzymatic degradation of the cellular glycocalyx, on cellular adhesion dynamics. To quantitatively characterize the underlying mechanical stimuli, computational fluid dynamics (CFD) simulations were performed to estimate fluid velocity fields and shear stress distributions within the custom well geometry. Our results identify a distinct shear stress regime in which cellular adhesion is enhanced, followed by higher mechanical force levels that lead to a reduction in adhesion strength. These findings provide a new experimental framework for probing flow-dependent cellular biophysical responses at the single-cell level and contribute to a deeper understanding of adhesion regulation in physiologically relevant flow environments.

1. Introduction

To understand key biological processes – both physiological and pathological – such as vascular diseases, organ development, or immune responses, it is crucial to model the mechanical environment of cells. Cell adhesion is a key biological process in which cells bind to each other or to a substrate through a variety of receptor-ligand interactions [1–3]. During this fundamental change, the involved cells undergo significant morphological changes [4]. Different proteins, receptors, and ligands are involved, depending on whether the adhesion is cell-cell or cell-extracellular matrix (ECM), as they are generated through distinct cellular mechanisms. When a cell attaches to another cell, it does not necessarily flatten; instead, it maintains a more rounded structure due to the balance between adhesive forces, which pull the cell outward, and internal contractile forces trying to pull it inward [5]. The shape of the cell is dictated by the dynamic remodeling of these forces. However, when a cell attaches to the ECM, it typically flattens and expands horizontally because integrins and other focal adhesions firmly attach the cytoskeleton to the substrate. The spreading of the cell provides a more stable mechanical connection with the ECM [6]. This extended contact

* Corresponding author.
** Corresponding author at: Nanobiosensorics Laboratory, Institute of Technical Physics and Materials Science, Centre for Energy Research, HUN-REN, Budapest, Hungary.
E-mail addresses: bonyar.attila@vik.bme.hu (A. Bonyár), horvath.robert@ek.hun-ren.hu (R. Horvath).
[1] Equal contribution as first author

https://doi.org/10.1016/j.snb.2026.141027
Received 21 May 2026; Received in revised form 18 September 2026; Accepted 1 October 2026
Available online 14 October 2026
0925-4005/© 2026 Elsevier B.V. All rights are reserved, including those for text and data mining, AI training, and similar technologies.

area not only stabilizes the cell but also increases its resistance to shear forces, which are commonly encountered under physiological in vivo conditions. Shear stress is a mechanical force that arises when a fluid moves along a surface, exerting a tangential force per unit area. In the human cardiovascular system, this mechanical force is primarily generated by the blood flow acting on the vessel-forming endothelial cells. Generally, the magnitude of the shear stress τ $\left(\frac{dyne}{cm^2}\right)$ is determined by the dynamic viscosity η of the blood and the velocity gradient $\frac{du}{dy}$ near the vessel wall as given in Eq. 1.

$$\tau = \eta \cdot \frac{du}{dy} \tag{1}$$

Where η $\left(\frac{dyne \cdot s}{cm^2}\right)$ is the dynamic viscosity of the blood, $\frac{du}{dy}$ is the rate of the change of velocity perpendicular to the vessel wall, typically expressed in $\frac{1}{s}$.

However, it is important to note that the shear force does not only depend on the speed of the blood flow and the dynamic viscosity of the blood, but also on the elasticity and the smoothness of the vessel wall [7]. This is particularly relevant in biological systems because the luminal side of the endothelial cells lining the inner wall of blood vessels is covered by a carbohydrate-rich matrix called the endothelial glycocalyx layer (EGL) [8]. The glycocalyx is a complex carbohydrate layer with a thickness ranging from 0.5 to 4.5 μm, present in a variable thickness on the surface of numerous cell types, including endothelial cells, as well as within the vascular system, the ducts of the respiratory tract, and certain leukocyte subpopulations [9–11]. It plays a pivotal role in antigen presentation, facilitating intercellular communication, mechanical defense, and immunological protection. It facilitates the so-called rolling adhesion of leukocytes to the vascular wall, and in tumor lesions, a thicker glycocalyx helps to protect cancer cells against immune responses [12]. In the nervous system, it appears at synaptic connections between individual neurons and enhances communication between cells. In contrast, its dysfunction can be related to neurological diseases, as well as Alzheimer's disease [13]. Enzymatic hydrolysis of the glycocalyx can better model certain pathological conditions [14]. The EGL is composed of various negatively charged saccharides, such as sulfated glycosaminoglycans (e.g., heparan sulfate) and sialoglycoproteins [15]. It plays a crucial role not only in endothelial barrier function but also acts as a mechanotransducer, transmitting signals that induce morphological changes in the cell [16,17]. Glycosaminoglycans exhibit kosmotropic behavior due to their negatively charged, highly polar nature because of the sulfate and carboxyl groups, which attract water molecules and promote the formation of an ordered water structure around them [18]. This ordered water phase contributes to the ability of glycocalyx to provide protection to the endothelial cells while reducing shear stress and aiding blood flow in blood vessels under physiological conditions.

To study both physiological and pathological conditions, in vitro cell culture is a widely used and indispensable tool in modern biology and medicine. By selecting appropriate experimental methods, cell and tissue types, we can obtain a satisfactory and cost-effective alternative to animal experimentation, but not a substitute. Regarding fluid flow, there are static and dynamic models of cell culture, which differ primarily in the transport of nutrients, oxygen, and the mechanical forces acting on the cell culture [19,20]. Although static models are versatile tools for monitoring cellular interactions, microbial pathogenesis, drug effects, or pathomechanisms, as well as conducting pharmacological, physiological, or pathological studies, their major drawback is that, due to the lack of fluid flow, the acting mechanical force – shear stress – is not present in these systems and therefore they cannot adequately model the biomechanical effects that affect cells in their natural environment [21]. The absence of shear stress alters cell morphology, adhesion, signaling, and gene expression, which are all particularly important in immunological, cancer, and vascular research [22,23].

Therefore, dynamic systems that provide fluid flow and shear force may provide more accurate and physiologically relevant results. Dynamic cell culture techniques, which have come to the fore in the last decade, have fundamental advantages but require longer and more careful field trials than their static counterparts [24]. A number of in vitro models are available to facilitate comprehension of physiological conditions. One such model involves culturing cells in a flow field, thereby enabling the modeling of different flow patterns (laminar, turbulent, oscillatory) [25]. In in vitro experiments, preconditioning of the cells under investigation is typically conducted following exposure to shear stresses ranging from 1 to 20 dynes/cm^2 [26].

One of the simplest models is the Parallel Plate Flow Chamber, in which cells are grown on a PDMS surface and a pump is used to generate specific flow velocities and shear stresses in the culture chamber [27]. This method provides a uniform flow field, but does not model the three-dimensional geometry of the blood vessels and the pulsatility of the vessel wall. Another obvious solution is a system based on the principle of generating a shaking, tilting fluid flow or the cone-and-plate system, which is relatively easy to implement but does not provide the user with enough control over the parameters and primarily provides only endpoint measurements [28,29]. The cone-and-plate flow chamber utilizes a cone that rotates within a static space to maintain uniform flow, thereby generating consistent shear stresses on the cells and thus offering a more accurate approximation to physiological conditions. However, this configuration presents the disadvantage of complicating the microscopic examination of cells within the system. The most advanced technology in this field is the so-called lab-on-a-chip microfluidic device, which enables precise control of flow rates through microchannels and has the capability to capture dynamic cellular responses in real-time. However, the extreme advantages of this device have one major drawback: the complexity of the system itself [30]. These channels are capable of modeling the three-dimensional structure of the vessel walls with a high degree of accuracy, allowing for the study of individual cellular interactions. However, the precise control of shear forces remains challenging.

To address these limitations, we have attempted to combine the advantages of previous approaches with as little downside as possible, developing a customized commercial label-free biosensor system where fluid rotation within the well allows a precise shear stress application. This system offers high spatial and temporal resolution, as well as real-time imaging via evanescent wave-based detection for examining cell behavior under flow conditions, while still allowing the validation of cell morphology and position using conventional optical microscopy [31,32]. In addition, recent years have seen a growing emphasis on increasing the resolution of various cell kinetic studies to be able to observe single-cell kinetics [33,34]. This paradigm shift, which is moving the research world from the population-level cellular studies to the analysis of signals at the single-cell level, can only be achieved with the right tools. Technological advances and the application of new methods enable cells to be analyzed individually rather than as a group, revealing the complexity of biological systems in greater detail and precision [35]. Biosensors with extremely high spatial resolution, capable of measuring cells at the microscopic level, in real-time under various conditions, play a key role in this process [36]. It is essential to note that transitioning to single-cell resolution does not preclude the continuation of population-level studies. By averaging and aggregating single-cell data, traditional population analyses can be reinstated, thereby providing the opportunity to build consistent and detailed pictures for studies at various levels [37]. This development therefore complements, rather than precludes, population-level studies, allowing accurate single-cell analysis and wider use of aggregated data from these studies.

Table 1
Summary Table of the Various Fluidic Platforms.

Platform	*Parallel-plate flow chamber (PPFC)*	*Cone-and-plate*	*Lab-on-chip / microfluidic system*	*RWG biosensor with magnetic liquid-rotation*
Dynamic shear range	~0.01 – 30 dyn/cm^2 (physiological range) [45]	Broad range, 1 – 12 dyn/cm^2, cone-and-plate rheometry strain rate 0.1 – 100000 s^{-1} [46]	Very wide range – up to ~ 1600 dyn/cm^2, 929-fold tunable in a single chip [47]	Rotation 1000 – 3000 rpm; CFD-simulated fluid velocity 0 to ~1.16 m/s (shear not quoted in dyn/cm^2) [48]
Spatial resolution	Monolayer field (~cm^2), uniform region within ~ 5% if aspect ratio ≤ 20:1 [49]	Whole-plate field, radial gradient option, ~ 4% of cells in central, non-uniform zone [50]	Single-cell, sub-cellular via channel geometry, models 3D vessel wall	25 μm (high-resolution Epic) / 83 μm (Benchtop); 2 x 2 mm sensors, 150 nm evanescent sensing depth [51,52]
Temporal resolution	Real-time (limited by microscopy)	Real-time possible but microscopy limited by rotating cone	Real-time, high (video microscopy)	3 s (Benchtop) / ~ 12 s (high-resolution BT) [48]
Throughput	Low – one condition per chamber	Moderate (multi-well variants)	Variable: single-cell force methods, 5 – 10 cells/day, adhesion chambers reach hundreds [53]	High – 12 wells in parallel on 384-well plate; up to ~ 1200 individual cells per session [52]
Single-cell resolution	No (population/monolayer)	No	Yes (trapping/single-cell channels)	Yes (25 μm pixels resolve single cells)
Key advantages	Well-defined laminar shear, simple, reproducible, easy microscopy [54]	Uniform, well-defined shear, closer to physiological conditions, simple	Precise flow control, real-time, 3D geometry, single-cell, low reagent use	Label-free, real-time, single-cell and population from one dataset, combines shear application with biosensing, plate-compatible
Key limitations	2D only, no vessel geometry or pulsatility, > 80% stress variation from end effects without confinement, low parallelization [54]	Primarily endpoint, difficult in-situ microscopy, secondary/edge flows, central non-uniformity	Fabrication complexity, PDMS/ flow-control overhead, lower parallelization than plate formats	Requires CFD calibration; no 3D vessel geometry

1.1. Biosensors

The study of dynamic changes in biophysical parameters at the single-cell level often requires the application of biosensors with high spatial and temporal resolution [38]. Optical biosensors provide an optical field in which the processes occurring are investigated on the basis of light phenomena (e.g., diffraction, refraction, interference) [39]. Sensing is based on the interaction between the optical field and the bio-recognition component. Label-free technologies do not use any other signal-amplifying molecule; thus, the analyte can be processed in its intact form [40]. Optical biosensors, of which the resonant waveguide grating (RWG) biosensor is an example, function based on the analytic components in the evanescent field, inducing a refractive index change in the local region of the sensor surface, thereby altering the resonance and converting the illuminating light into a different wavelength component with different resonance frequencies in the grating waveguide layer [41]. This phenomenon is known as near-surface dynamic mass redistribution (DMR). The resonant wavelength component subsequently propagates for a brief period within the layer before exiting via reflection, and is then detected by a complementary metal oxide semiconductor (CMOS) camera.

In the present study, we used the Corning EPIC Cardio high spatial – single-cell level resolution – RWG biosensor, which provides a lateral spatial resolution of 25 μm on a 2 mm x 2 mm sensor surface, providing highly detailed data on cellular interactions and adhesion kinetics [42]. The EPIC Cardio biosensor is a tool based on resonant waveguide grating technology that enables real-time and label-free monitoring of cells. Its principle of operation is based on the evanescent field phenomenon, where light arriving at the sensor surface resonates at a specific wavelength, generating an evanescent wave that extends only a very short distance from the boundary [43]. This wave has rapidly decaying amplitudes and does not transport energy, but it is highly sensitive to refractive index changes in the 150 nm vicinity of the sensor surface, making it ideal for non-invasively detecting molecular interactions and cellular processes [44].

A table comparing the key parameters of various fluidic systems used for laboratory and research purposes with those of fluidic systems incorporating the optical biosensor that yielded the results of this study is provided below (Table 1).

1.1.1. The hemodynamic forces in the cardiovascular and the lymphatic system

The fluids that fill the unique fluid spaces in the human body, as well as the cardiovascular and lymphatic systems, exhibit different flow characteristics in different regions of the body. The flow velocity of the fluid space and the mechanical forces exerted on each compartment, such as shear forces and surge forces, are influenced by both the solid and dissolved components present in the fluid being transported [55]. Adhesion interactions have been demonstrated to play a role in the development of certain diseases and in the health of the body. This has been evidenced by the precipitation of an altered intrinsic structure, for instance in the case of cancer cells along the vascular walls, or the phagocytotic activation of monocytes in the interstitial space [56]. Upon exit of phagocytes and some lymphocytes from the vasculature, adhesion molecular interactions between specific adhesion molecules, integrins, cadherins, selectins, and receptors on endothelial cells that form the vascular walls facilitate their passage into the interstitium [57]. It has been hypothesized that the aberrant expression of specific adhesion molecules may play a role in promoting cell proliferation within the vascular wall, instigating inflammation, and contributing to the onset of autoimmune diseases [58]. The flow rate of fluid spaces is primarily determined by their viscosity, which is also influenced by the presence of dissolved ions, antibodies, platelets, red blood cells, and leukocytes [59]. The elasticity of the cells and their dynamic morphological changes contribute, e.g., to their passage through capillaries, where only a single red blood cell can fit in some regions [60,61]. The tangential forces exerted on the vessel walls, i.e., the lymphatic vessels, are known as shear forces. The flow profile can be laminar, where the fluid flows at the fastest speed in the center of the blood vessels, and the speed decreases as it approaches the vessel wall [62,63]. While the blood flow throughout the cardiovascular vessels is largely laminar, chaotic advection and transitional flows frequently arise due to the pulsatile nature of the cardiac cycle and are amplified at sites of vessel deformations, including normal arterial bifurcations and pathological features like aneurysms or atherosclerotic lesions.

The endothelial cells come into direct contact with the blood flow. The flowing blood stimulates the endothelial cells, which in response secrete various substances, such as nitric oxide (NO) or prostacyclin [64]. It has been demonstrated that high shear forces influence the

function of endothelial cells and the quality of the extracellular components of secreted substances, thereby contributing to the regulation of their function [65]. Prolonged exposure to high shear forces has been shown to induce NO production, which in turn relaxes blood vessels. Furthermore, prolonged high shear forces have been demonstrated to activate mechanotransduction pathways and induce increased expression of certain genes [66]. Prolonged exposure to high shear forces has been shown to lead to endothelial cell degradation. The regions exhibiting the lowest shear stresses are those along vascular bifurcations, where the development of atherosclerosis is more probable [67]. In the case of oscillations in shear force, proinflammatory responses may be induced, which may in turn trigger the adhesion of monocytes and some lymphocytes. Mechanosensory receptors with different functions are expressed on endothelial cells. Integrins sense through the extracellular matrix, PECAM-1 (Platelet Endothelial Cell Adhesion Molecule-1) transmits mechanical signals to the intracellular space, VE-cadherins enhance intercellular connections, quasi-stabilizing the vascular wall structure, while ion channels, such as Piezo-1 and TRPV4 receptors, regulate calcium ion uptake [68–70]. In the presence of oxidative stress, endothelial cells exert anti-inflammatory effects by producing NOX2 and NOX4 NADPH oxidases [71,72].

1.1.2. Insight into single-cell adhesion studies

The study of adhesion interactions at the single-cell level is an extremely complex undertaking, yet also of fundamental importance in many areas of life science research. The biomolecules involved in cell adhesion include cadherins, integrins, selectins, and immunoglobulins [73,74]. Adhesion molecules bind to cytoskeletal actin filaments through focal adhesion complexes (FAs) [75]. Cadherins are responsible for intercellular coupling, while integrins are responsible for adhesion to the extracellular matrix [76]. Selectins and immunoglobulins are involved in the immune response and the vascular network [77,78]. In tumor lesions, individual cells detach from their tissue, i.e., cell-cell cadherin junctions are reduced, and epithelial-mesenchymal transition is enhanced [79].

The functionality of the monitored surface can vary depending on the nature of the experiments. To mediate cellular adhesion, surface functionalization could be a possible approach. The arginine-glycine-aspartic acid (Arg-Gly-Asp or RGD) motif is an extracellular oligopeptide that is capable of controlling the cellular adhesion mechanisms that are key to the activation and clustering of integrin proteins, which play a fundamental role in cell adhesion, spreading, and signaling during various biological processes [80–82].

2. Materials and methods

2.1. Cell culture

The HeLa cell line was used for the measurements (Fig. 1b). The cells were maintained in an incubator at 37 °C in a humidified environment with 5 V/V% CO_2. Dulbecco's Modified Eagle's Medium (D-MEM) was used to maintain the cell line, supplemented with 10 w/V% fetal calf serum. In addition, 4 mM L-glutamine, 100 U/mL penicillin, and 100 μg/mL streptomycin were used in the culture medium. The density of the HeLa cell suspension used for our measurements proved to be ideal when 2500 cells were used in a final volume of 600 μL (i.e., at a density of about 4100–4200 cells/mL); at this density, we achieved signals at the single-cell level but observed adhesion phenomena over most of the entire sensor surface.

2.1.1. The sensor surface functionalization

The biosensor (Fig. 1a) signal baseline was performed using a 10 mM HEPES/MQ water buffer solution, normally run for 20 min (Fig. 1c, e). Functionalization of the sensor surface was carried out using a graft copolymer of 100 μg/mL poly-L-lysine-polyethylene glycol and poly-L-lysine-polyethylene glycol-RGD (Arg-Gly-Asp) mixed at a 1:1 ratio, for 40 min, with the sensor wobbled, and then the functionalization was examined for 30 min until saturation of the wavelength shift signal. The well was washed 3 times with 10 mM HEPES/MQ water buffer, and then a cellular baseline was recorded and assayed using cell culture medium, i.e., D-MEM, for 30 min.

2.1.2. Enzymatic hydrolysis

The chondroitin-6-sulfate, chondroitin-4-sulfate and dermatan sulfate components of the glycocalyx layer of the HeLa cells were hydrolyzed using chondroitinase ABC enzyme (Fig. 1d, e). Enzymatic hydrolysis was performed for 45 min by adding the enzyme to the cell suspension, adjusting the enzyme activity to 0.6 U/mL. Enzymatic hydrolysis was terminated by removing the supernatant and washing the well with 10 mM HEPES/MilliQ buffer.

2.1.3. Rotation of cellular supernatant

After the enzymatic digestions (or without enzymatic hydrolysis), the suspension was rotated immediately after the cell adhesion phase (Fig. 1e). The short- and long-term effects of several rotation speeds between 1000 and 3000 rpm on cell behavior were investigated.

2.1.4. Plate-holder and rotating mechanism

The experimental setup utilized a customized plate holder and a rotation mechanism to generate fluid rotation over the biosensor array (Fig. 2a, b). The plate holder was designed so that the sensor plate was accessible in wells with the following dimensions: each well was 8.8 mm wide and 10.65 mm deep with two precisely positioned 2 mm x 2 mm sensors on the well centerline, equidistant from the center of the well with four additional sensor segments arranged in a matrix pattern, two above and two below the main sensors, partially extending beyond the well boundaries (Fig. 2c). To generate the required flow field, a rotating magnetic stirrer was placed over the closed wells, with a magnetic stirrer bar carefully positioned underneath the light barrier top coat. The dimensions of the stirrer bar were 6 mm in length and 2.95 mm in width. Although static magnetic fields can influence cell behavior at moderate intensities ($\geq$ 1 mT) or during prolonged exposure [83–85], in our experimental setup, the drive magnet and the stirring bar are located at the top of the ~10.65 mm liquid column. Consequently, the magnetic field at the sensor surface decreases to the level of the ambient weak field ($<$ 1 mT), so direct magnetobiological effects are negligible during our short (~1 h) rotation phases [86].

2.1.5. Viability test, epifluorescent imaging, and image processing

Cellular viability was assessed using the Invitrogen ReadyProbes™ Cell Viability Imaging Kit (Blue/Green; Thermo Fisher Scientific). Briefly, 16 μL of the reagent was added to the culture supernatant prior to epifluorescence imaging.

Microscopy was performed using an Axio Observer Z1 inverted microscope equipped with an LD Plan-Neofluar 20x/0.4 Corr Ph2 M27 objective. For phase contrast imaging, a halogen light source was used (3.4 V) with an exposure time of 10 ms. Fluorescence imaging was carried out using Filter Set 02 (ex: 335–383 nm; em: $>$ 420 nm) with a 190 ms exposure time, and Filter Set 38 (ex: 450–490 nm; em: 500–550 nm) with a 280 ms exposure time. Images were acquired using an Axiocam 705 monochrome camera coupled with a 0.63x adapter. Image processing, including single-cell segmentation and counting, was performed using the 'cyto3' model of the Cellpose algorithm on both phase-contrast and epifluorescence images.

2.1.6. Biosensor data evaluation

The biosensor features a 2 x 2 mm^2 active sensing area with a spatial resolution of 25 μm, resulting in an 80 x 80 pixel image per sensor scan. The measurement system simultaneously acquires data from 12 sensors arranged in a 3 x 4 array. During data acquisition, the system exports a video tensor with dimensions (T, 240, 320) for each experiment, where T denotes the total number of temporal measurements. This tensor is

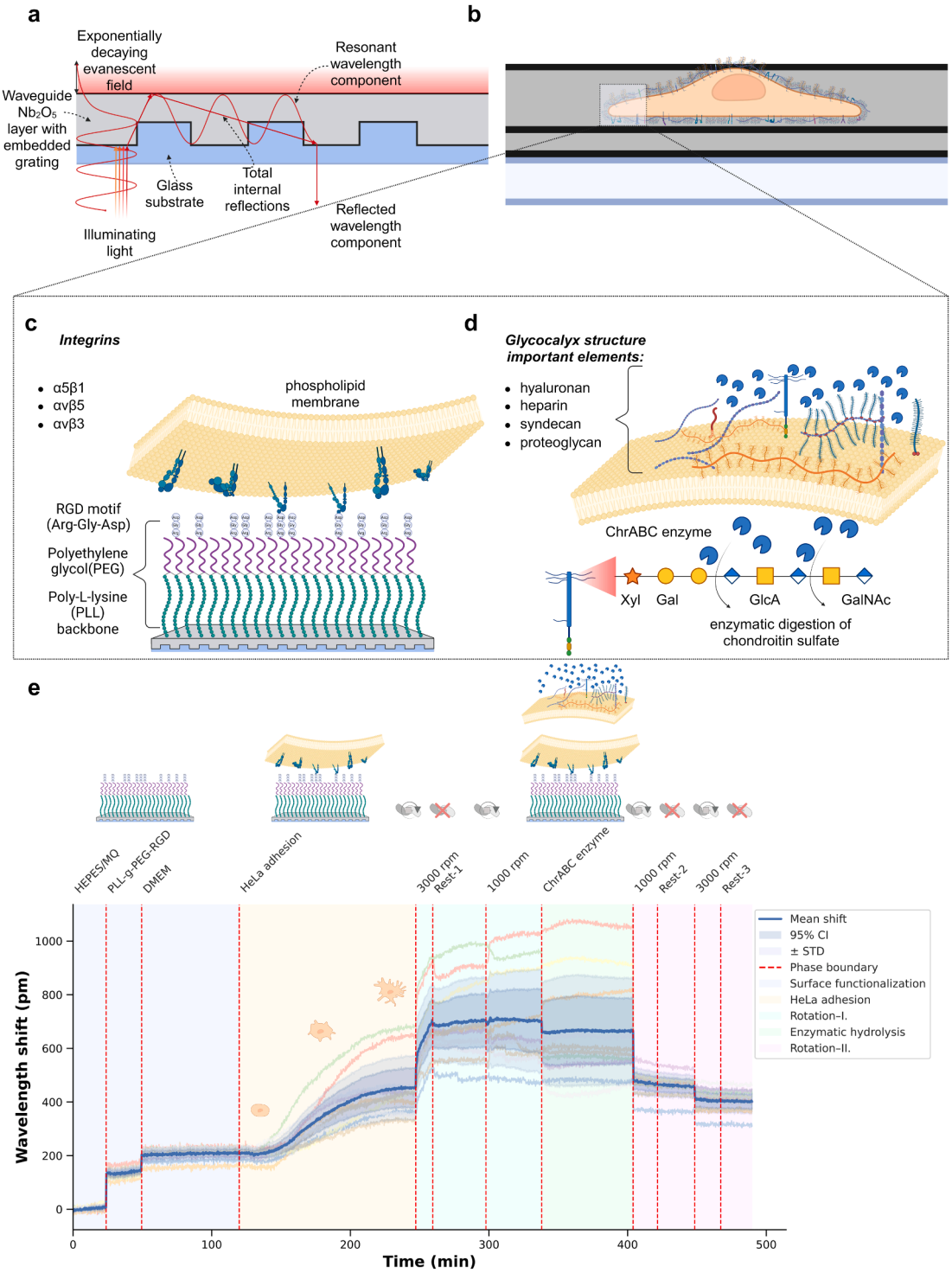


Fig. 1. Schematic illustration of the key phases of our measurements. a) Operating principle of the high spatial resolution RWG biosensor. b) Schematic diagram of individual HeLa cell adhesion. c) The sensor surface was functionalized with a 1:1 dilution of poly-L-lysine and polyethylene glycol graft copolymer modified with an RGD (Arg-Gly-Asp) motif (PLL-g-PEG-RGD) and PLL-g-PEG. d) Digestion and structural representation of the cellular glycocalyx layer. e) Representative measurement showing the recorded wavelength shift dataset over time (undersampled). The kinetics summarize all possible phase transitions discussed in the article. Initially, the sensor was incubated with 10 mM HEPES/MQ buffer, followed by functionalization of the sensor surface with PLL-g-PEG-RGD solution, after which the cellular baseline was established using Dulbecco's Modified Eagle's Medium. This was followed by an adhesion assay with HeLa cells, during which they progressively adopted the spread morphology characteristic of final adhesion, while the adhesion kinetics exhibited a sigmoidal profile. The cells were subjected to mechanical stress by rotating the assay medium using a floating magnetic stirrer bar at 3000 rpm. This was followed by a resting phase (rest-1) and subsequent rotation at 1000 rpm, after which the partial digestion of the cellular glycocalyx layer was examined using the enzyme chondroitinase ABC. We then applied rotation at 1000 rpm, followed by a second resting phase (rest-2), and subsequently examined the cells at 3000 rpm. The measurement was concluded with a resting phase (rest-3). Each phase is highlighted with a different background color. Additionally, the average wavelength shift of the representative, undersampled curves, along with their 95% confidence interval, and standard deviation, are indicated with shaded bands. Created in BioRender. Sallai, I. (2026) https://BioRender.com/b9iow2p.

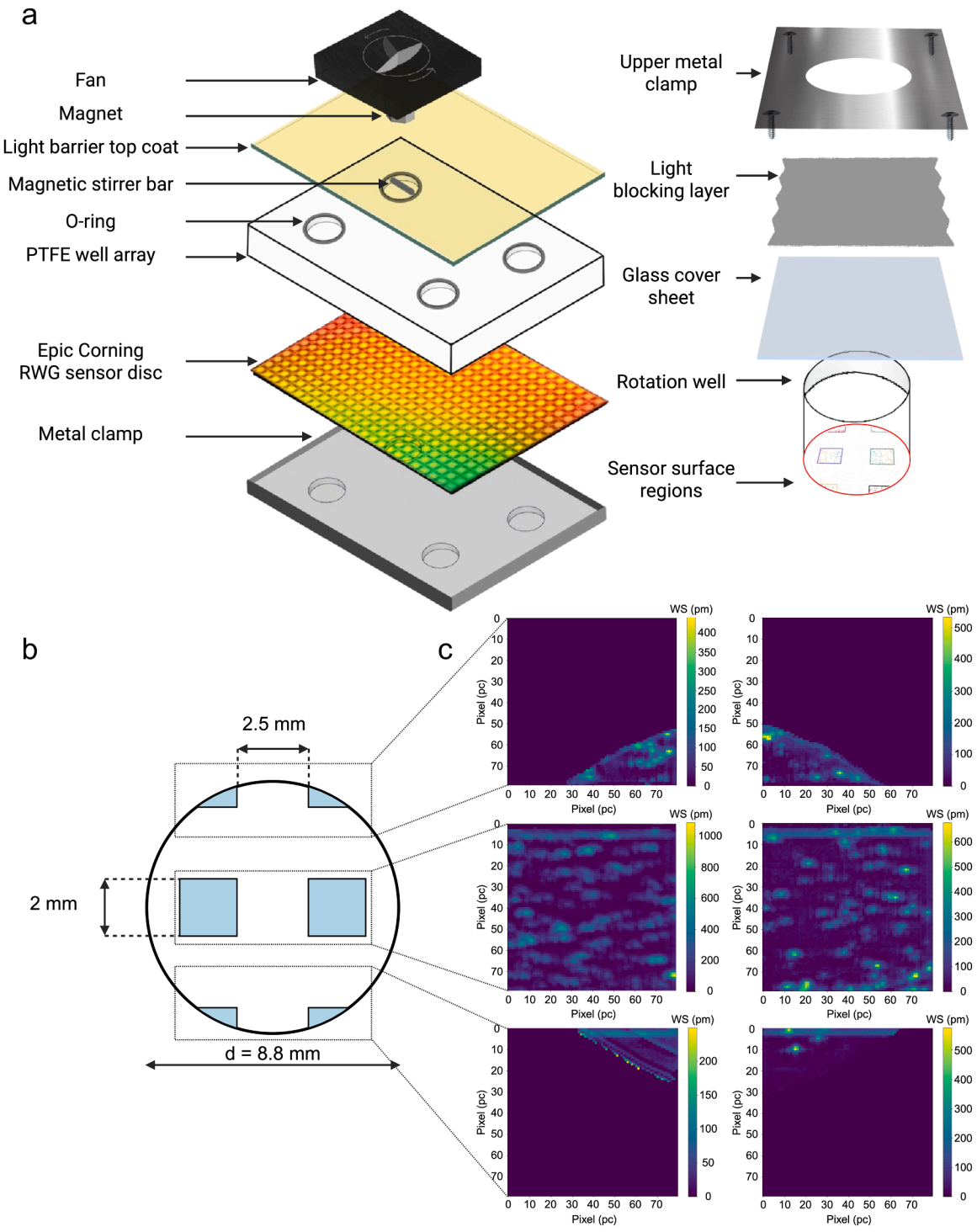


Fig. 2. Diagram showing the investigated measurement platform. a) The custom-made well plate and the attachable sensor plate. We insert a sensor element into a metal holder, onto which we place the Teflon (PTFE) well plate, which we designed using O-rings and incorporating an overflow channel. The uniform rotation of the liquid is ensured by a magnetic rotating bar floating in the working medium, which is secured by a magnet positioned above the light-blocking layer. The magnet is attached to a fan, which ensures uniform rotation and causes the magnetic bar to rotate without direct mechanical connection, simultaneously rotating the liquid space. To hermetically seal the fluid chamber, an object plate is used under the light-blocking layer, which is also coated with a light-blocking layer to prevent unwanted external illumination. The system is stabilized with the help of an upper metal clamp and fixing screws. b) A total of 6 sensor elements can measure wavelength shift signals in the custom-made well. Two sensor elements hang completely into the custom-made well, while four sensor elements hang partially into it. The sensor elements have an area of 2 mm x 2 mm, with a distance of 2.5 mm between adjacent sensor elements in the x and y directions. Our custom-made well has a diameter of 8.8 mm. c) The wavelength shift (WS (pm)) heat map generated by the sensor elements located in the custom-made well, i.e., the lateral inhomogeneous wavelength shift heat map with an area of 80 x 80 pixels (1 pixel = 25 x 25 μm^2) is displayed in pm resolution, with the individual sensor element pixels colored according to the maximum wavelength shift values recorded during the measurement.

subsequently partitioned into individual well representations of size (T, 80, 80).

Each well-specific time series is then truncated to align with the onset of the cell adhesion phase, which is determined from the biosensor timeline. Following this step, a three-stage signal correction procedure is applied. First, an offset correction is performed by subtracting the initial frame (t_0) from all subsequent frames. Pixels whose values exceed a maximum threshold of 5000 pm are then masked across the entire time series. Next, a manual background correction is applied by averaging the time series of user-defined background pixels and subtracting the resulting background signal from all pixel time series within the well.

After background correction, single cells are identified using a local-maximum–based peak detection approach. To enable this, each well tensor is collapsed into a single image by computing the per-pixel maximum across time. Standard local maxima detection is then applied, augmented with lower and upper absolute peak thresholds to suppress noise and outlier signals. For each detected peak, the corresponding time series is extracted from the preprocessed video tensor. These signals undergo a final manual filtering step to ensure that they represent valid single-cell responses and are then exported for subsequent analysis.

2.1.7. CFD simulation method

Numerical computations were carried out using the commercially available finite volume solver, ANSYS CFX 2024 R2. The well was modeled according to the experimental specifications as an 8.8 mm diameter cylinder with a length of 10.65 mm. The magnetic stirrer bar was represented by a cylindrical capsule shape that is 6 mm long and 2.95 mm wide. The numerical geometry was divided into a rotating fluid domain and a stationary domain to facilitate the simulation of the stirrer's movement.

The numerical mesh contained approximately 5 million tetrahedral cells, enhanced with five prismatic layers adjacent to the walls for accurate resolution of the boundary layers. Critically, the mesh near the bottom of the well achieved a fine resolution of 10 μm to precisely capture the near-field fluid behavior around the HeLa cells. The fluid was modeled using the properties of water, and the Shear Stress Transport (SST) turbulence model was utilized. Both temporal and spatial discretization schemes were set to Second Order for high accuracy. No-Slip boundary conditions were assumed for all wall boundaries and the magnetic stirrer bar surface.

The simulation strategy involved two stages. It was initiated with a steady-state frozen rotor simulation, which ran for approximately 1000 iterations until a periodically convergent solution was reached. This was followed by a transient simulation employing a sliding rotating body interface until a periodic flow solution was fully achieved. Simulations were conducted for stirrer speeds of 1000, 1500, and 3000 rpm, with corresponding total transient simulation times of 2.4, 1.6, and 0.8 s, respectively. For evaluation, twenty timesteps were exported from the last two complete rotations of each transient simulation to analyze the velocity field on a slice located 10 μm above the bottom of the well.

3. Results and discussion

3.1. Optimization of methodological principle based on parallel analysis of CFD simulation and cellular wavelength shift responses

We developed a complex framework for interpreting mechano-chemical responses. Our goal was to interpret single-cell responses and explore their biological significance. Using our fluidic rotation system, we analyzed the response signals of cells to mechanical influences at multiple rotation frequencies by adjusting the frequency of the rotation system, which was placed upon the RWG sensor. In the second phase of our experiments, we compared our unique cellular response signals obtained by partial digestion of the adhesive cells' glycocalyx layer with chondroitinase ABC enzyme, as well as the effect of simultaneous rotation and enzymatic digestion on cell behavior.

To classify single-cell responses, wavelength shift signals were analyzed by performing pairwise comparisons of adjacent measurement sections. Single-cell signals capture adhesion dynamics via real-time tracking of the resonant wavelength shift, providing a continuous and uniform temporal representation of cellular behavior. Fig. 3 shows the development and validation of the optimized wavelength shift signal evaluation framework. To distinguish viable cells from non-viable ones, we introduced a discrimination threshold of 50 pm, corresponding to the amplitude of background artifact signals. Signal variances for background ($n = 20$) and viable cell ($n = 142$) populations are presented in Fig. 3b, utilizing undersampling to address sample size disparity. We compared specific time windows extracted from the experimental phases to establish response categories. This analysis relies on the recorded wavelength shift dataset illustrated in Fig. 3a, where cellular adhesion precedes a controlled, non-destructive magnetic rotation stage. We created six unique cellular response categories based on the percentage change in the median wavelength shift of the baseline interval compared to the median of the treatment interval. We compared the terminal 20 min of the adhesion phase with the initial 5 min of the rotation phase. In contrast, for enzymatic digestion, the analysis encompassed the entire duration of the enzymatic phase. Cells whose wavelength shift signal fell below 50 pm were classified as 'Detached'. In addition, we created the following cell response categories: High increase (>15%), Low increase (+3% to +15%), Stable (±3%), Low decrease (–15% to −3%), and High decrease (< −15%) based on the medians of the compared time windows.

To elucidate the biophysical relationship between the simulated velocity mesh and the measured single-cell responses, the velocity magnitudes were spatially aligned with the wavelength shift time series data. A four-member so-called fitness score (S_f) had to be defined in Eq. 2 for this purpose. The optimal relative orientation was determined by maximizing the S_f across a full 360° rotation. Preliminarily, the velocity field rotation was inspected with 1–2–5–10° step sizes. The fits examined with finer increments (1–2–5°) yielded negligible improvements in S_f. The smaller angle rotation steps also risked overfitting to stochastic experimental noise. Nevertheless, to balance the overfitting and the model robustness, a 10° rotation step size was applied. The fitness score integrates four weighted metrics. The correlation term (C) evaluates the dependence between flow velocity and cellular response. For the calculation, Pearson or Spearman coefficients were utilized based on an initial examination of the linearity and monotonicity between the velocity and the cellular response at 0° alignment. The hypothesis term (H) quantifies adherence to the biophysical expectation that high velocities drive cell detachment (negative wavelength shift signals), while low velocities favor adhesion (positive wavelength shift signals). Additionally, radial consistency (R_c) assesses signal coherence among cells at similar radial distance, while the radial effect (R_e) accounts for distance-dependent response variations. Weight factors were assigned a priori to prioritize statistical strength and physical plausibility. The correlation term was dominant ($w_{corr} = 0.5$) to maximize the predictive power of mechanical stress. The hypothesis term ($w_{hyp} = 0.3$) ensured physical validity by rewarding regions where high shear correlates with detachment. Finally, radial metrics were assigned lower weights ($w^c_{rad} = w^e_{rad} = 0.1$) to penalize local variance and account for radial trends.

$$S_f = (w_{corr} \cdot C) + (w_{hyp} \cdot H) + (w^c_{rad} \cdot R_c) + (w^e_{rad} \cdot R_e) \quad (2)$$

In Fig. 3c, we compare the two correlation methods, Pearson and Spearman, for all measurement settings where we always moved from an adhesion, resting, or enzymatic digestion phase to a rotation phase, both for concentric and offset simulations. The analysis shows that the points are closely aligned along the y = x line, indicating that we obtained similar results with both correlations, which confirms the robustness of the fitness score calculation. Based on the fitness score, we determined which simulation resulted in a more ideal fit between the concentric and offset simulations for a given phase transition. We also

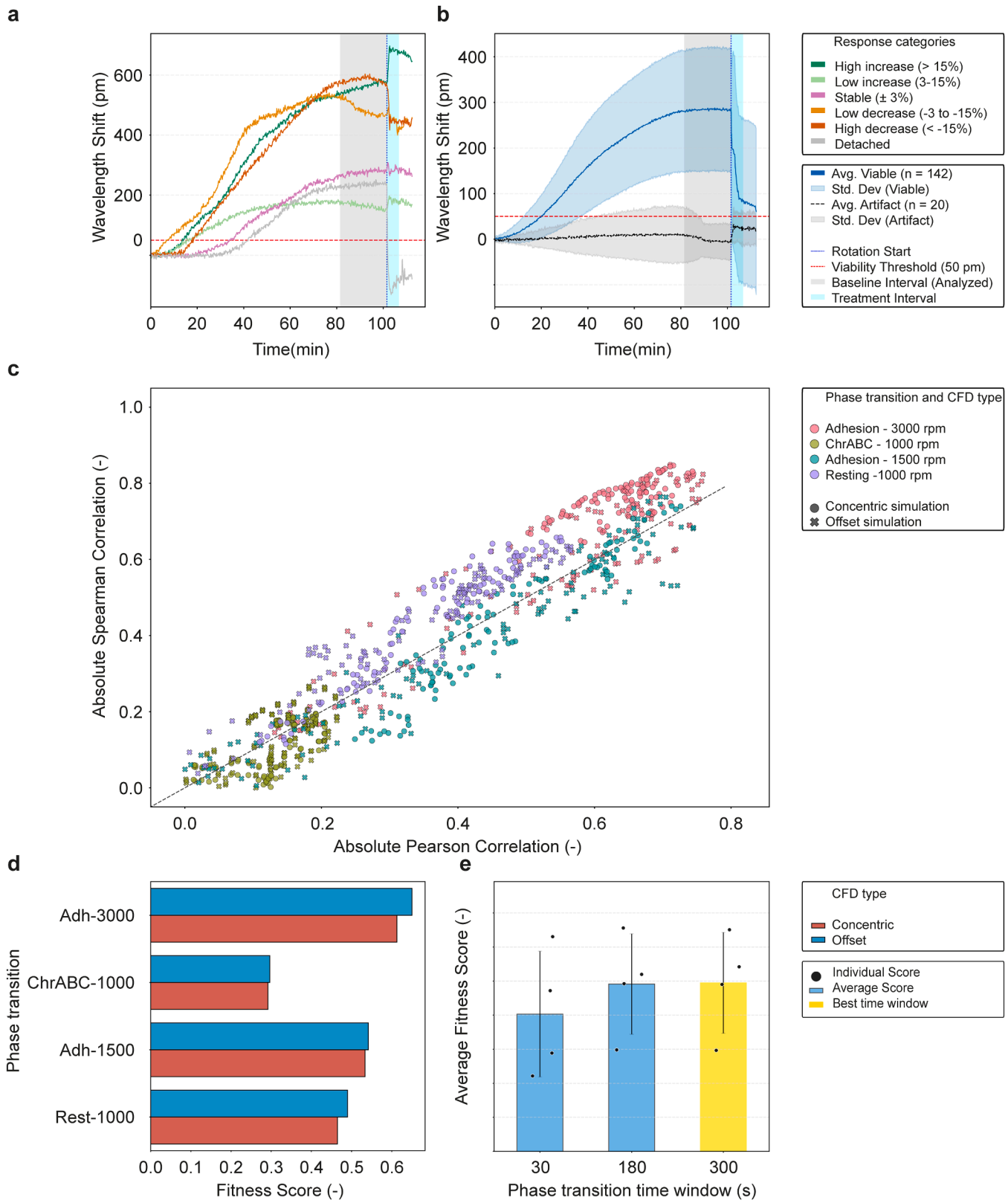


Fig. 3. Presentation of the validation algorithm for the analysis process of the mechanobiological relationship and optimization of the analysis parameters. a) Examples of individual cellular response signals from the six types of cell categories identified. Comparison of the median of the 1200 s adhesion phase of the gray "Baseline interval" with the median of the first 300 s time window of the rotation phase indicated with a light blue band ("Treatment interval"). b) Diagram showing the definition of the 50 pm viability wavelength shift threshold. The blue curve is the curve averaged from the total cellular signal of the Adhesion → 1500 rpm phase transition, with values consistently above 50 pm. Artifact signals are marked in black. c) Diagram showing the Pearson and Spearman correlation tests. The scoring metric shows robustness (R^2 >0.9) for both correlation methods. d) Comparison of simulation types based on fitness score when examining different rotational phase transitions. e) Optimization of the test duration of the rotational measurement phase based on the average fitness score, comparing intervals of 30–180-300 s.

used the average fitness score to determine the optimal rotation time window, which we calculated from the average of the fitness scores of all rotation experiments, as shown in Fig. 3d. The analysis was performed for time windows of 30–180–300 s as shown in Fig. 3e. The 300 s time window resulted in the highest average fitness score. This confirms that the most stable relationship between the biological response signal and physical stress develops within 5 min.

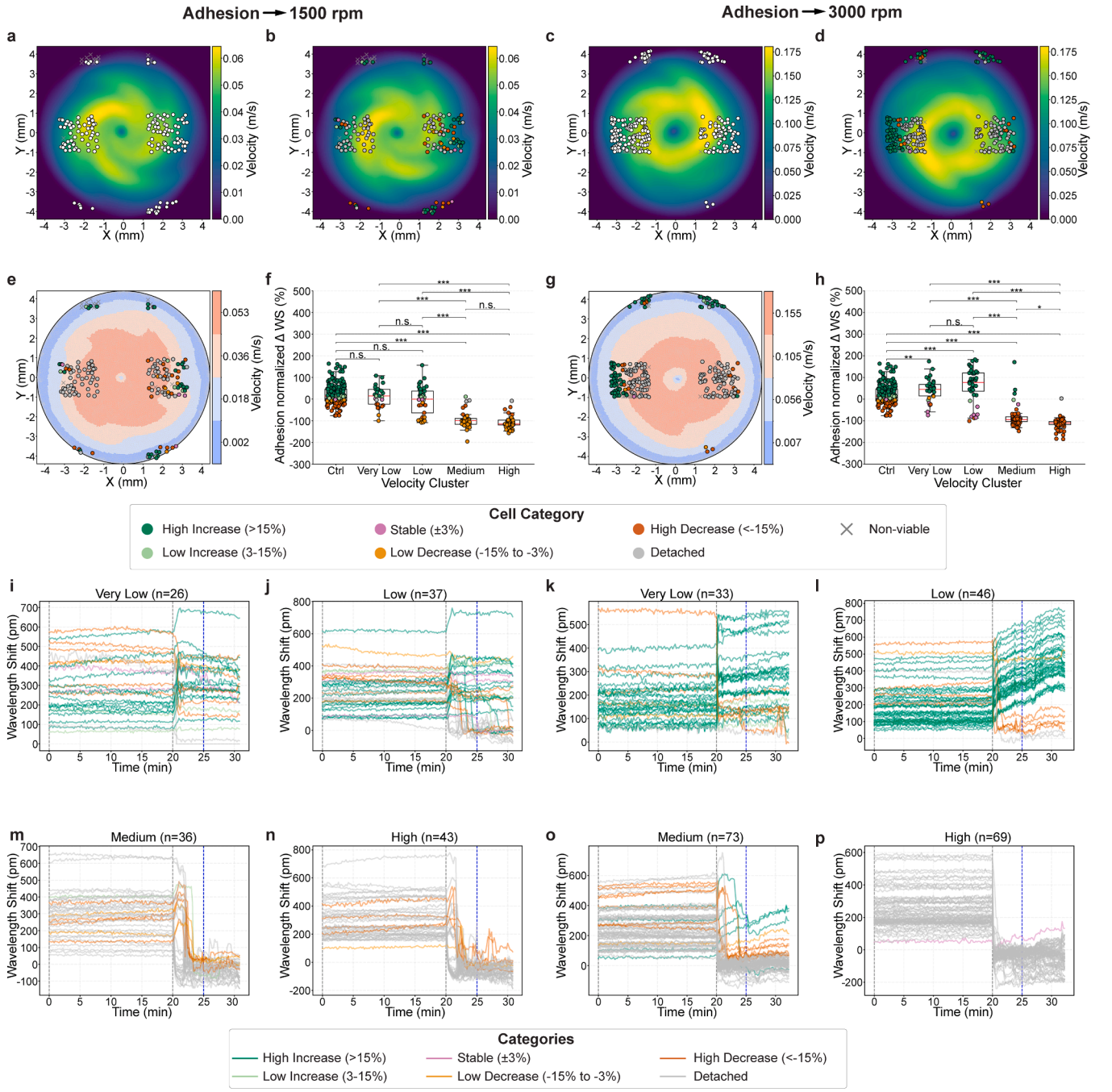


Fig. 4. CFD simulated velocity fields and properties of individual cell response signals for the Adhesion → 1500 rpm and Adhesion → 3000 rpm phase transitions. Diagrams a, b, e, f, i, j, m, n) are related to the Adhesion → 1500 rpm phase transition, and diagrams c, d, g, h, k, l, o, p) are related to the Adhesion → 3000 rpm phase transition. a, c) Velocity magnitudes of the CFD simulation at each point of the simulation mesh applied to the well. The cells are marked with independent white markers, and non-viable cells are marked with gray Xs. b, d) Cell positions, marked with colors corresponding to cell response categories, are shown on the flow velocity field rotated based on the fitness score and fitted to the cell response signals. e, g) The grid obtained after space division using Voronoi tessellation on the discrete simulation point set, with segments colored according to the 4 velocity cluster regions obtained after adaptive K-Means clustering. Cells marked with the color of the cell response category and the corresponding marker are also shown on the clustered velocity field. f, h) Delta wavelength shift normalized by the median wavelength shift of the last 20 min of the adhesion phase (the difference between the median wavelength shift for the first 5 min of the rotation phase and the median wavelength shift for the last 20 min of the adhesion phase, expressed as a percentage) along the velocity field clusters, indicating the p values determined by the χ^2 test. i-p) The individual cell wavelength shift curves located in each velocity cluster are plotted as a function of time, marked with the color corresponding to the cell response category. The borders of the two compared phases are marked with gray and blue dashed lines respectively, and the cell numbers belonging to the clusters are also indicated.

3.2. The effect of different rotation frequencies

The effects of rotation frequencies of 1500 rpm and 3000 rpm applied after the adhesion phase were evaluated (Fig. 4). We present the original simulation without fitting the velocity field (Fig. 4a, c), where the spatial positions of the cells are marked and cells that are not alive at the boundary between the two phases are removed. In the rotated velocity field, we marked the cells with colors and markers corresponding to the cell response category type (Fig. 4b, d). The fitness score, ideal rotation angle from the original velocity magnitude map, and the correlation values applied are marked in the boxes above the figures. To map the discrete simulation points to the continuous physical reality, we employed Voronoi tessellation, generating a continuous flow field coverage. Crucially, as cells are spatially extended entities rather than point masses, mechanical load is distributed across their entire basal contact surface. To align this with our sensor resolution – where a 25 x 25 μm^2 pixel captures the signal of a representative cell – we calculated the effective velocity by averaging the field within a 25 x 25 μm^2 area centered on each cell. However, the surface representing the cells may consist of several Voronoi regions at the same time, which in certain cases can be classified into different clusters. As a result, the physical position of the cells may differ from the statistical analysis presented in the boxplot diagram. Instead of imposing arbitrary geometric boundaries (e.g., fixed rings or circular segments), we employed adaptive K-Means clustering to partition the velocity field based on data similarity. For each cell, we calculated the local velocity magnitude by averaging the simulation mesh values within the corresponding 25 x 25 μm^2 pixel area. This data-driven approach classified the flow environment into four distinct regions: 'High', 'Medium', 'Low' and 'Very Low' velocity clusters. The scaling used is relative, since, e.g., at 1500 rpm, the mean value of the High velocity cluster is 0.053 m/s, while at 3000 rpm it is 0.155 m/s (Fig. 4e, g). The clusters of the two phase transitions cannot be matched in absolute terms, but they clearly show the dynamics within the system.

The ratio of High- to Low-increase response categories was unexpectedly elevated at 3000 rpm compared to 1500 rpm. This discrepancy arises from the differential survival of adherent cells. At 3000 rpm, cells in High and Medium velocity clusters undergo widespread detachment, restricting the remaining population to strongly adhering cells in the Very Low (0.007 m/s) and Low (0.056 m/s) zones. Conversely, at 1500 rpm, shear forces are not always sufficient to overcome cellular adhesion, resulting in a diverse spatial distribution where even weakly adhering cells remain attached in High velocity regions. This indicates a transition from a region dominated by biological heterogeneity at 1500 rpm to one driven by deterministic mechanical stress at 3000 rpm, characterized by sharp response differentiation. We analyzed differences in cell category distributions across velocity clusters using a Chi-squared (χ^2) test of independence, as both the velocity field cluster and cellular response category classification are categorical variables (Fig. 4f, h). Our null hypothesis (H_0) assumed that cellular response categories are independent of the local velocity region, while the alternative hypothesis (H_1) expected a significant correlation. P-values indicate a stronger category separation at 3000 rpm compared to 1500 rpm. Outliers above +200 and −200% normalized wavelength shift values were excluded. Control measurements were also performed; in these experiments, we did not use rotation, but only conducted a longer-term adhesion test (Figs. 4f-4h marked as Ctrl). For this analysis, cellular responses were evaluated within two specific time windows: the initial adhesion phase (T1, 70–90 min) and the intervention phase of the continued unperturbed adhesion (T3, 178.8–221.2 min). Normalization was performed using the median value of the T1 segment, and the delta wavelength shift was calculated from the difference between the median values of the two segments being compared. We compared the different time periods of adhesion and examined the cell category distribution, as well as whether the cell category distribution observed in the individual speed clusters of the control and rotation measurements showed a significant difference. At 1500 rpm, the cell category distribution in the Very Low and Low velocity clusters did not differ significantly from that of the control group, whereas the distribution of cells in the Medium and High velocity clusters showed a significant difference. In contrast, at 3000 rpm, the control group showed a significant difference compared to the cell category distribution in all velocity clusters. A detailed explanation of the control group analysis can be found in Figure S1.

All single-cell traces are displayed in Fig. 4i-p. The ending times of the compared phases are marked with gray (adhesion) and blue (rotation) dashed lines, respectively. Notably, cells in the 'Low increase' and 'Detached' categories frequently exhibit a transient, rapid surge in wavelength shift at the onset of rotation (spanning approximately 1 min or 4–5 data points). This initial positive excursion likely results from hydrodynamic compression, effectively pressing the cells against the sensor surface. Furthermore, the velocity field clustering algorithm successfully stratifies these distinct kinetic signatures, revealing clear phenotypic divergence between cells in the Low versus Medium velocity regions.

Local flow velocity-dependent cell status variation is detailed in Fig. 5. At 1500 rpm, the spatial distribution of detached cells exhibits high variability with significant overlap between 'Attached' and 'Detached' populations in the velocity field (Fig. 5a, c). In contrast, 3000 rpm induces a clear bimodal segregation (Fig. 5b, d), where attached cells are confined to low-velocity regions and detached cells correspond to high-velocity regions, indicating a strict physical dependence on local shear stress.

A Mann-Whitney *U* test (non-parametric, two-sample) confirmed a statistically significant difference in local average velocities between the two cell statuses. To characterize the cellular response, we plotted the normalized wavelength shift (normalized by the median of the last 20 min of the adhesion phase) against average velocity (Fig. 5e, g). Furthermore, we analyzed detachment kinetics by partitioning the velocity space into 15 discrete iso-velocity intervals (Fig. 5f, h). Within each interval, we calculated the local detachment probability. This analysis allowed us to identify a critical hydrodynamic threshold, above which the local detachment rate significantly exceeds the global average. These findings confirm that detachment is systematic rather than random.

Analysis of individual detachment profiles reveals a distinct time-dependent adhesion fatigue at 1500 rpm, characterized by a slower initial decay (~3 min) compared to the rapid rupture observed at 3000 rpm (Fig. 5i-p). These temporal traces directly underpin the Kaplan-Meier survival (Figure S3) estimates, which quantify the instantaneous probability of the 'Attached' versus 'Detached' states. Under low mechanical stress, the non-linear detachment kinetics suggest that cells engage in active mechanoadaptive reinforcement to counteract the shear force. Ultimately, our objective was to distill the complex biological heterogeneity into two distinct, binary mechanical phenotypes.

3.3. The effect of enzymatic digestion of chondroitin-6-sulfate, chondroitin-4-sulfate, and dermatan sulfate glycocalyx components on cellular behavior, based on RWG biosensor and phase contrast microscopy measurements

To investigate the interplay between mechanical history and glycocalyx integrity, we compared cellular responses following enzymatic digestion either directly after adhesion or after high shear stress conditioning (3000 rpm) (Fig. 6). Our results reveal that prior mechanical stress significantly sensitizes cells to enzymatic degradation. In the group pre-exposed to rotational stress, the combined proportion of 'Detached' and 'High decrease' categories reached 77%, compared to only 27% in the adhesion-only control (Fig. 6a). Conversely, mechanically naive cells primarily exhibited stable or increasing signals (aggregating to ~65%), whereas these resistant groups of cells were suppressed to < 25% following mechanical stress (Fig. 6b).

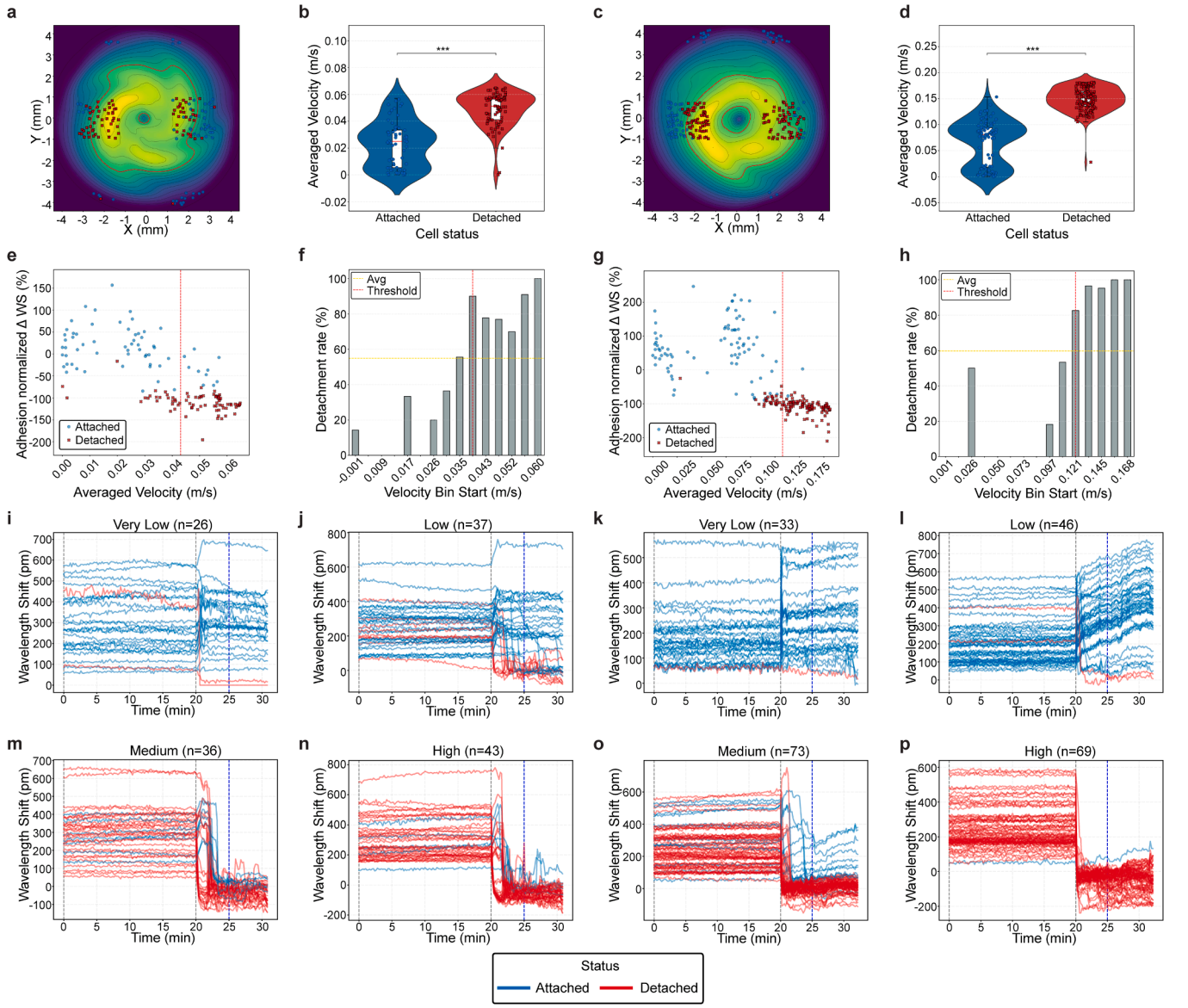
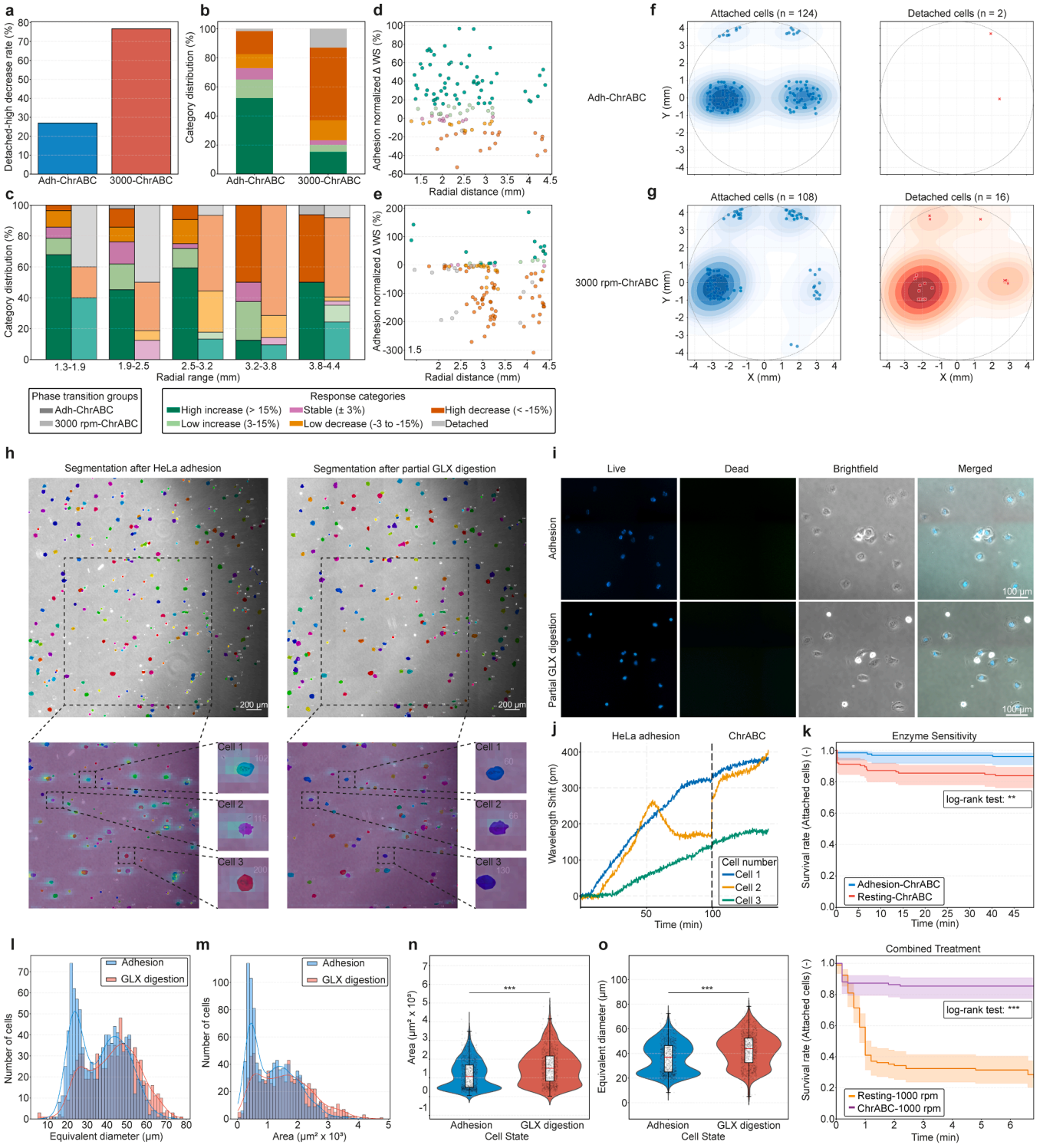


Fig. 5. Results of cell status-based analysis. Diagrams a, b, e, f, i, j, m, n) are related to the Adhesion –› 1500 rpm phase transition, and diagrams c, d, g, h, k, l, o, p) are related to the Adhesion –› 3000 rpm phase transition. a, c) Representation of the flow field recorded with ideal rotation, showing the set of points with the same velocity by indicating "lines of force." The positions of individual cells are marked with blue spheres and red x markers, indicating their detached or attached status. Only the set of points classified as viable cells at the beginning of the given phase transition is presented. The detachment threshold force line is shown as a red closed shape. b, d) Average velocity (velocity magnitude averaged over a 25 μm x 25 μm area accepted as a cell) represented by violin plots based on cell status (Mann-Whitney *U* test, *p* values indicated). e, g) Delta wavelength shift normalized by the median wavelength shift of the last 20 min of the adhesion phase (percentage difference between the median wavelength shift of early rotation (first 5 min) and late adhesion (last 20 min)) plotted as a function of the average velocity. The detachment threshold velocity is indicated with a dashed red line. f, h) Depiction of detachment rate (%) for all 15 velocity ranges, indicating the average detachment and threshold values. i-p) The individual cellular wavelength shift curves are shown as a function of time, with colors corresponding to the cell status.

Spatially, we observed no radial dependence in cell category distributions for either condition, confirming that – unlike shear stress – enzymatic activity exerts a spatially homogeneous effect (Fig. 6c). Analysis of normalized wavelength shifts revealed substantial intercellular variability, particularly within the 'High increase' category for direct digestion and the 'High decrease' category for the group pre-exposed to rotational stress (Fig. 6d-e).

Spatial density heatmaps have been created for visualizing the topography of the cellular responses according to the ’Attached’ and ’Detached’ cell statuses (Fig. 6f-g). The analysis of the adhesion-only control (ChrABC after adhesion) indicated spatially independent distribution. The enzymatic digestion resulted in minimal detachment (n = 2) and the adhesion-strengthening effect was predominant. In contrast, applying partial digestion of the glycocalyx after 3000 rpm mechanical stress revealed a strong spatial dependence in the wavelength shift signals in the case of cells with both Attached (n = 108) and Detached (n = 18) status. The heatmap reveals a distinct segregation. The 'red zones,' representing the highest density of enzymatically detached cells, were concentrated in specific regions, whereas 'blue zones,' corresponding to cells with increased adhesion, were preferentially localized in the radially peripheral zones. This indicates that while enzymatic digestion mediates an overall adhesive reinforcement, prior mechanical stress at 3000 rpm promotes detachment and creates a radially stratified response pattern.



(caption on next page)

Fig. 6. Parallel analysis of enzymatic digestion based on cell response category distribution, and microscopic analysis. a) Evaluation of the effect of chondroitinase ABC enzyme applied after the adhesion phase and after the 3000 rpm rotation phase based on the ratio of Detached and High decrease cell categories. b) Distribution of individual cell categories in the case of enzymatic digestion after adhesion and after 3000 rpm rotation. c) Distribution of cell response categories marked with the colors of each cell category along the radial range in the case of enzymatic digestion after adhesion and after 3000 rpm (columns without fading and columns with fading). d-e) Relative delta wavelength shift response (%) for enzymatic digestion after adhesion and after 3000 rpm, plotted as a function of radial distance (mm) with cell categories color-coded. f-g) Diagrams representing the response signal density after adhesion and after enzymatic digestion at 3000 rpm. h) Results of segmentation performed with the Cyto3 model of the CellPose algorithm on cells appearing in the entire custom-made well after adhesion and enzymatic digestion (20x microscope objective, brightfield images, Zeiss Axio Observer Z1 phase contrast microscope), supplemented with wavelength shift heat maps aligned with phase contrast microscopic images of the sensor regions and three selected cells after adhesion and enzymatic digestion are segmented and aligned. i) Fluorescence, brightfield, and merged images of cells stained with Invitrogen ReadyProbes™ stains for viability testing. NucBlue® Live reagent (suitable for staining live cells, which stains the cell nucleus; excitation/emission maximum: 360/460 nm) was suitable for detecting live cells using a DAPI fluorescent filter set, while NucGreen® Dead was ideal for staining nuclei with damaged plasma membranes (excitation/emission maximum: 535/617 nm), which is suitable for emission spectrum detection with Filter Set 38 (ex: 450–490nm; em: 500–550nm). j) The wavelength shift characteristics observed during cell adhesion and enzymatic hydrolysis in the three segmented examples. k) Survival kinetics were plotted as a function of treatment time, both for enzymatic digestion and for enzymatic digestion followed by rotation at 1000 rpm. The log-rank test was applied for testing significance. l-m) Cell numbers plotted as a function of equivalent cell diameter and adhesion cell surface area, analyzed using brightfield microscopic images after adhesion and enzymatic digestion. n-o) Violin plots showing the equivalent diameter and adhesion cell surface area of segmentation masks analyzed after adhesion and after enzymatic digestion, with significance levels determined using the Mann-Whitney *U* test.

To analyze the potential cytotoxicity of the applied enzyme, we performed brightfield phase contrast and epifluorescence imaging post-adhesion and post-digestion (Fig. 6i). Cellular viability was assessed using the Invitrogen ReadyProbes™ Cell Viability Imaging Kit (Blue/Green). Total nuclei were visualized with the NucBlue® Live reagent (ex/em: 360/460 nm) using Carl Zeiss Filter Set 02, while membrane-compromised non-viable cells were identified via the NucGreen® Dead reagent using Filter Set 38 (ex: 450–490 nm; em: 500–550 nm). Quantitative analysis confirmed $< 1\%$ non-viable cells across all conditions, demonstrating that enzymatic digestion alters cellular mechanics without compromising viability. Morphological analysis was conducted on brightfield images using the Cellpose3 algorithm (cyto3 model), with manual curation of segmentation masks to ensure accuracy (Fig. 6h). We quantified the equivalent diameter and projected adhesion area for each cell, applying a size-exclusion filter (5–80 μm) to eliminate artifacts and aggregates. Consistent with our wavelength shift data, enzymatic treatment induced significant cell spreading. Statistical analysis (Mann-Whitney *U* test, $p < 0.001$) revealed a significant increase in both equivalent diameter and cell area following partial digestion of the glycocalyx, as illustrated by the shift toward larger phenotypes in the corresponding violin diagrams and histograms (Fig. 6l-o). Following segmentation of phase contrast microscopic images, we aligned them with the sensor image of lateral inhomogeneous wavelength shift signals after both the adhesion phase and the enzymatic hydrolysis phase, in which we identified unique wavelength shift signals assignable to segmented cells. Fig. 6h shows the images matched with the sensor image and the curves of three cells in Fig. 6j, which show that cell adhesion increased during enzymatic hydrolysis, as indicated by the increasing trend.

Finally, we analyzed survival kinetics to quantify the percentage change in cell retention under combined stress sequences. Comparing enzymatic digestion post-adhesion versus post-mechanical stress (3000 rpm) revealed a sequence-dependent effect: cells subjected to mechanical preconditioning exhibited significantly lower survival rates than the adhesion-only control ($p = 0.001$, log-rank test) (Fig. 6k). This suggests that high-shear stress accelerates the kinetics of subsequent enzymatic degradation. Furthermore, we contrasted this with a reverse sequence, where enzymatic digestion preceded mechanical loading (at a lower intensity of 1000 rpm). The survival analysis demonstrated that chemical degradation prior to mechanical stress results in the most severe viability loss, significantly exceeding the detachment observed in the combined 'mechanical-then-chemical' scenarios ($p < 0.001$). This confirms that intact glycocalyx is critical for resisting shear forces, and its prior removal renders cells highly vulnerable even to moderate mechanical loads.

3.4. Investigation of single-cell level adhesion kinetics based on post-digestion mechanical stress of glycocalyx in cases previously exposed and not exposed to mechanical stress

To distinguish the synergistic effects of mechanical and chemical stress, we monitored adhesion metrics across two distinct experimental sequences using chondroitinase ABC. In the first protocol, to test for shear-induced sensitization, cells were subjected to high-intensity rotation (3000 rpm) prior to enzymatic digestion. In the second protocol, to assess glycocalyx-mediated structural integrity, enzymatic digestion was applied immediately post-adhesion (followed by a conditioning resting phase), after which the cells were exposed to a reduced rotational frequency of 1000 rpm. This lower frequency was selected based on the hypothesis that partial removal of the glycocalyx would render cells critically vulnerable even to moderate shear forces. Our primary objective was to determine whether prior high-shear conditioning (3000 rpm) accelerates the kinetics of subsequent enzymatic rupture, contrasting this with the scenario where enzymatic degradation precedes rotational mechanical treatment.

Cells depicted in Fig. 7a, b, e, f retained viability following the sequential application of 3000 rpm shear stress and enzymatic digestion. Conversely, the cohort in Fig. 7c, d, g, h was subjected to glycocalyx digestion immediately after adhesion. Our results demonstrate that without the digested components of the glycocalyx layer, the structural competence of the cells (previously sufficient to withstand high-shear transitions) collapses. Even at the reduced frequency of 1000 rpm, we observed dramatic cell detachment. Crucially, this loss extended to low-velocity cluster regions, areas where detachment was negligible in intact controls even at 1500–3000 rpm (Fig. 7e, g). Boxplot diagrams reveal that the 'Detached' response category dominates across all velocity regions, effectively homogenizing the spatial distribution and erasing the cluster-specific differences observed in category distribution (Fig. 7f, h). With detachment velocities converging around $v_{det} \approx 0.005$ m/s, these data confirm that for partially glycocalyx-digested cells, 1000 rpm represents a supercritical shear condition, irrespective of prior mechanical history (Fig. 7b, d). Kinetically, the ChrABC to 1000 rpm transition is characterized by an immediate drop in wavelength shift at the onset of rotation, particularly in Medium and High velocity clusters (Fig. 7i-p). While the total detachment rate is comparable to the static digestion control (chemical stress only), the kinetics differ fundamentally: mechanical removal at 1000 rpm is instantaneous, whereas purely chemical detachment proceeds more gradually.

We evaluated cellular retention under a terminal 1000 rpm load following two distinct stress histories: (i) sequential mechanical conditioning (3000 rpm) followed by enzymatic digestion (Fig. 8a, b, e, f, i, j,

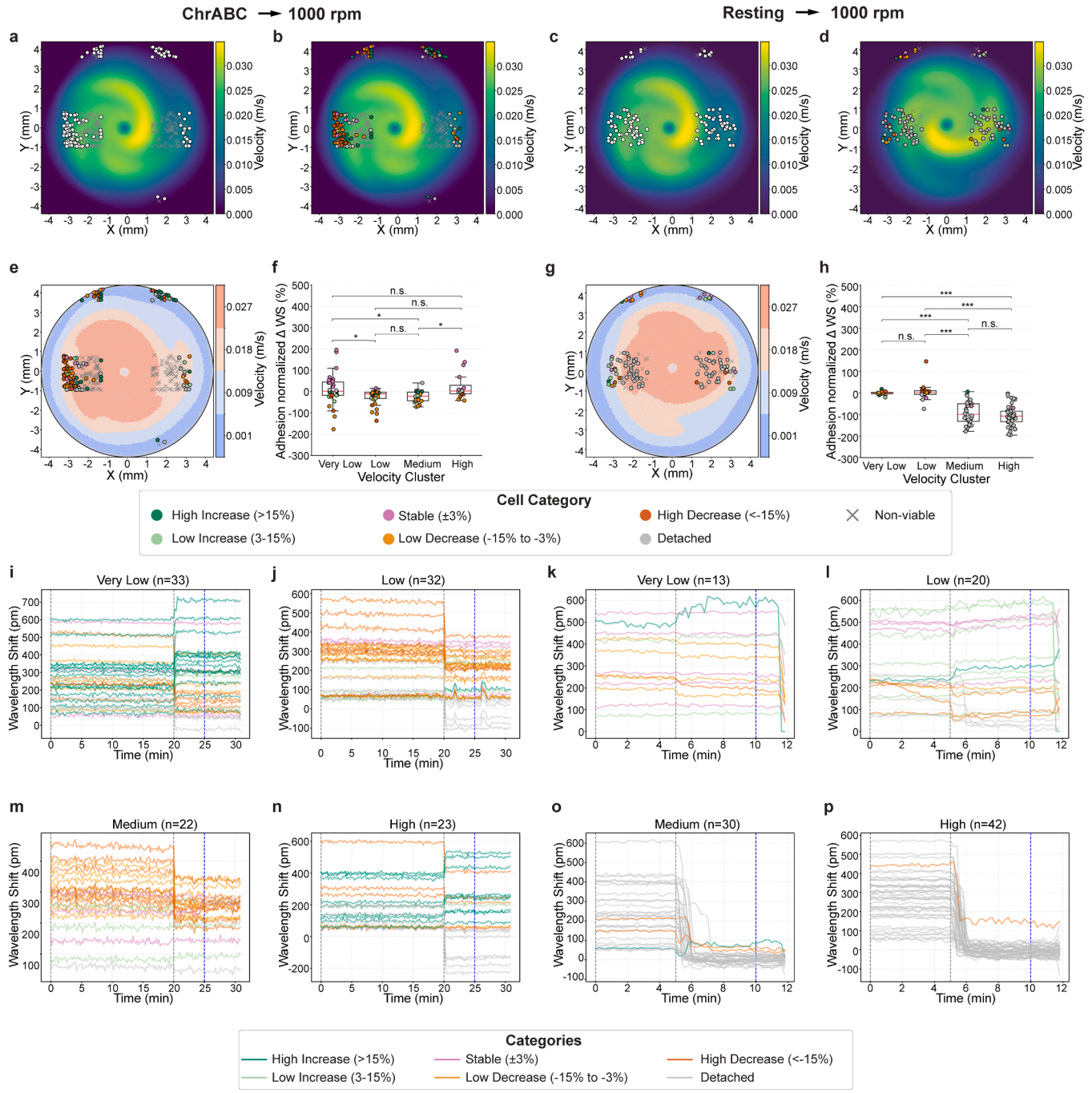


Fig. 7. CFD-simulated velocity fields and properties of individual cell response signals for the ChrABC → 1000 rpm and Resting → 1000 rpm phase transitions. Diagrams a, b, e, f, i, j, m, n) are related to the ChrABC → 1000 rpm phase transition, and diagrams c, d, g, h, k, l, o, p) are related to the Resting → 1000 rpm phase transition. a, c) Velocity magnitudes of the CFD simulation at each point of the simulation mesh applied to the well. The cells are marked with independent white markers, and non-viable cells are marked with gray Xs. b, d) Cell positions, marked with colors corresponding to cell response categories, are shown on the flow velocity field rotated based on the fitness score and fitted to the cell response signals. e, g) The grid obtained after space division using Voronoi tessellation on the discrete simulation point set, with segments colored according to the 4 velocity cluster regions obtained after adaptive K-Means clustering. Cells marked with the color of the cell response category and the corresponding marker are also shown on the clustered velocity field. f, h) Delta wavelength shift normalized by the median wavelength shift of the last 20 min of the enzymatic phase and the last 5 min of the resting phase (the difference between the median wavelength shift for the first 5 min of the rotation phase and the median wavelength shift for the last 20 min of the enzymatic phase/the last 5 min of the resting phase, expressed as a percentage) along the velocity field clusters, indicating the p values determined by the χ^2 test. i-p) The individual cell wavelength shift curves located in each velocity cluster are plotted as a function of time, marked with the color corresponding to the cell response category. The borders of the two compared phases are marked with gray and blue dashed lines, respectively, and the cell numbers belonging to the clusters are also indicated.

m, n), and (ii) direct enzymatic digestion after adhesion (Fig. 8c, d, g, h, k, l, o, p). In the sequential measurements, the survivor cells formed a distinct, highly resistant subpopulation. Despite the harsh pre-treatment, these cells exhibited a remarkably low detachment rate (15.5%) during the final 1000 rpm rotation (Fig. 8f). Crucially, statistical analysis revealed no significant velocity dependence ($p = 0.143$) between attached and detached cells (Fig. 8b). This suggests that for this selected group, the prior high-shear history supersedes the spatial

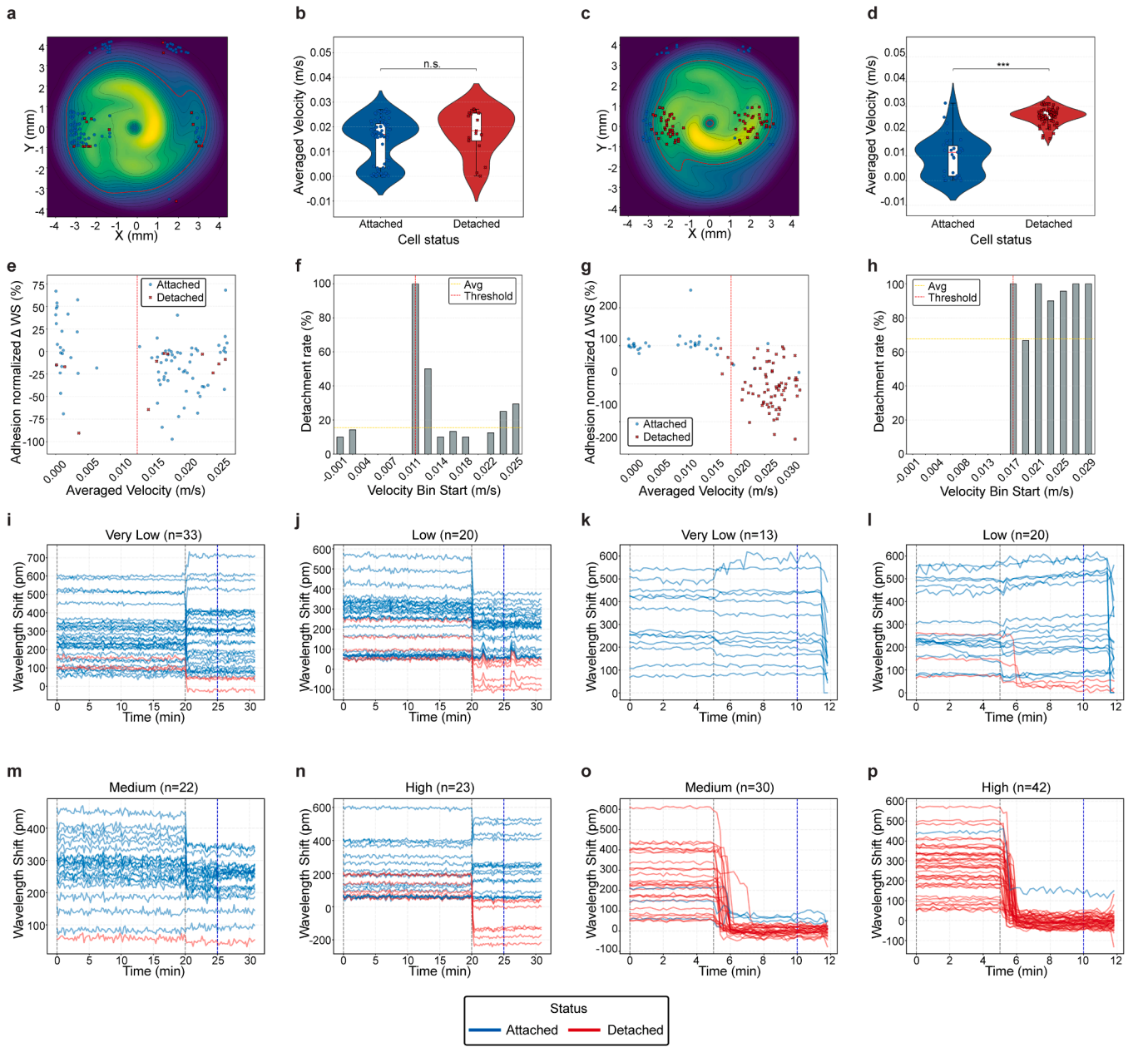


Fig. 8. Results of cell status-based analysis. Diagrams a, b, e, f, i, j, m, n) are related to the ChrABC → 1000 rpm phase transition, and diagrams c, d, g, h, k, l, o, p) are related to the Resting → 1000 rpm phase transition. a, c) Representation of the flow field recorded with ideal rotation, showing the set of points with the same velocity by indicating "lines of force." The positions of individual cells are marked with blue spheres and red x markers, indicating their detached or attached status. Only the set of points classified as viable cells at the beginning of the given phase transition is presented. The detachment threshold force line is shown as a red closed shape. b, d) Average velocity (velocity magnitude averaged over a 25 μm x 25 μm area accepted as a cell) represented by violin plots based on cell status (Mann-Whitney *U* test, *p* values indicated). e, g) Delta wavelength shift normalized by the median wavelength shift of the last 20 min of the enzymatic phase and the last 5 min of the resting phase (percentage difference between the median wavelength shift of early rotation (first 5 min) and the last 20 min of the enzymatic phase/the last 5 min of the resting phase) plotted as a function of the average velocity. The detachment threshold velocity is indicated with a dashed red line. f, h) Depiction of the detachment rate (%) for all 15 velocity ranges, indicating the average detachment and threshold values. i-p) The individual cellular wavelength shift curves are shown as a function of time, with colors corresponding to the cell status.

variations of the lower-frequency test; the calculated threshold of $v_{th} = 0.013$ m/s is thus statistically nominal (Fig. 8e). In sharp contrast, the direct digestion group displayed high vulnerability (67.6% detachment) and a rigorous spatial determinism (Fig. 8c, h). Here, detachment was strictly governed by local velocity ($p < 0.001$), characterized by a sharp, binary threshold at $v_{th} = 0.019$ m/s (Fig. 8d, h). Below this critical velocity, adhesion retention was ~99.9%, whereas regions exceeding the threshold exhibited ~100% detachment. This confirms that without prior mechanical selection, enzymatic digestion renders adhesion physically compromised, resulting in an 'all-or-nothing' manner driven purely by local shear stress.

The rigor of the sequential selection process – comprising high-frequency rotation (3000 rpm) followed by enzymatic digestion – likely isolated a mechanically recalcitrant subpopulation. Consequently, the subsequent 1000 rpm rotational stress proved insufficient to drive velocity-dependent differentiation within these highly resistant cells. While the reduced sample size of the survivor pool (n = 110) admittedly limits the statistical power of the Mann-Whitney U test, rendering it

underpowered to detect refined effects, this lack of statistical significance underscores a critical biological insight: the existence of a stress hierarchy. Whereas the initial adhesion-to-rotation transition was governed strictly by hydrodynamic parameters (making fluid velocity the primary predictor), the final phase is dominated by structural history. The population had already been purged of vulnerable cells; thus, retention in this phase reflects the intrinsic robustness of the survivors rather than the nuances of the local velocity field.

4. Conclusions

As previously noted in the summary of Table 1, although established macroscopic and microfluidic platforms provide precise shear force control or complex 3D geometries, they inevitably require a compromise between manufacturing complexity, high-throughput parallelization, and real-time single-cell resolution. The RWG biosensor applied in this study, coupled with magnetic rotation, aims to bridge this methodological gap by enabling the analysis of mechanical properties at the single-cell level across regions with multiple flow velocities, so-called velocity clusters, even if this requires computational fluid dynamics (CFD) calibration.

A high-throughput hydrodynamic platform has been developed that generates a continuous radial velocity gradient, creating a diverse spectrum of shear stress conditions simultaneously. By coupling this rotational setup with a high lateral spatial resolution resonant waveguide biosensor, we were able to precisely quantify single-cell responses elicited by the hydrodynamic treatment, bridging the gap between macroscopic fluid forces and microscopic cellular mechanics.

A unified analytical framework has been established for classifying cellular behaviors into six distinct response categories based on their kinetic signatures during sequential mechanical and enzymatic transitions. To spatially map these responses to physical forces, we employed Computational Fluid Dynamics (CFD) to model both concentric and offset flow scenarios. By maximizing a fitness score derived from the cell response distributions, we identified the optimal simulation model, thereby achieving a precise spatial registration between the theoretical velocity field and the empirical single-cell data.

At 3000 rpm, the average shear force in the rotational space immediately exceeds the tensile strength of the weaker binding forces. At the same time, the cells that withstood this intense physical impact and remained on the surface are likely to form a mechanically stable subpopulation that continues to show stable surface adhesion throughout the rest of the measurement, as indicated by the rapid onset of the plateau phase. In contrast, at 1500 rpm, the average shear force does not sort with the same intensity as at 3000 rpm, and the plateau phase sets in at around 5 min. Individual cell curves showing a slow gradual decline may indicate the exhaustion of RGD binding of adhesion proteins, while curves showing a sudden, almost vertical drop may indicate the immediate rupture of bonds.

The differential impact of enzymatic digestion has been evaluated based on the cells' mechanical history, comparing digestion immediately post-adhesion versus digestion following high-shear conditioning (3000 rpm). While enzymatic treatment of mechanically naive cells resulted in adhesion reinforcement, prior exposure to rotational stress significantly sensitized the population, leading to extensive detachment and weakening of adhesion. Notably, this detachment response strictly followed the spatial heterogeneity established by the preceding 3000 rpm velocity field. The persistent spatial pattern is consistent with a history-dependent effect, but the present design cannot distinguish active mechanomemory from enrichment of pre-existing shear/adhesion-resistant states; both mechanisms may contribute.

The comparative analysis highlighted the critical role of stress history in determining cellular fate. Two protocols – direct enzymatic digestion versus digestion preceded by high-shear conditioning (3000 rpm) – have been contrasted. In the absence of prior mechanical loading, the monolayer proved highly vulnerable; subsequent exposure to even gentle rotation (1000 rpm) resulted in a massive shift toward 'High Decrease' and 'Detached' categories. Conversely, the application of a preconditioning shear step (3000 rpm) isolated a mechanically recalcitrant subpopulation. Remarkably, this cohort – comprising cells that originally exhibited active adhesion reinforcement ('High/Low Increase') – maintained surface attachment throughout the subsequent enzymatic challenge and secondary rotation (1000 rpm). While their signal characteristics transitioned from 'Increase' to 'Low/High Decrease' states – reflecting the loss of chondroitin-sulfate components of the glycocalyx layer – their persistence on the surface confirms that the initial mechanical selection favored a phenotype with superior intrinsic adhesion stability.

The persistent spatial differences observed after flow conditioning are consistent with a history-dependent phenotype, but the present single-cell level design does not uniquely identify active cellular mechanomemory. Flow may instead, or additionally, enrich a pre-existing subpopulation with greater adhesion or shear resistance. Such mechanical selection is plausible because single cancer-cell populations show broad adhesion-strength distributions, including cell-cycle-dependent heterogeneity in HeLa cells, and because flow, adhesion, matrix stiffness, and constriction-based challenges can enrich tumor subpopulations with distinct metastatic or survival phenotypes [87–89]. Conversely, mechanical cues can also induce persistent YAP/TAZ-, microRNA-, and chromatin-associated states [90–92]. Resolving these alternatives will require pre-state-to-fate linkage – e.g., lineage barcoding or sister-cell transcriptomic profiling coupled to shear challenge–together with adhesion pre-sorting, washout, and rechallenge experiments [93,94].

Author contributions

Igor Sallai and Dános Sebestyén Varga developed the instrumentation and software, performed experiments, analyzed results, prepared figures, and wrote the manuscript. Benjamin Csippa performed computational fluid dynamics (CFD) simulations using Ansys and contributed to the writing. Bálint Béres developed code for processing raw DMR data and contributed to the writing. Zoltán Szittner assisted in the preparation of vector graphics for the figures. Inna Székács maintained the cell cultures. András Dér contributed to the discussions and to reviewing the manuscript. Robert Horvath and Attila Bonyár conceptualized the study, supervised the experiments and data analysis, contributed to funding acquisition, were responsible for data curation, provided resources, technical support, and supervised the project.

Declaration of Competing Interest

The authors declare that they have no known competing financial interests or personal relationships that could have appeared to influence the work reported in this paper.

Acknowledgments

This project was supported by the Momentum (Lendület) Program of the Hungarian Academy of Sciences and the National Research, Development, and Innovation Fund (NKFIH) of Hungary under grant TKP2021-EGA-04, ADVANCED 153121, and 2024–1.2.10-TÉT-IPARI-IL-2024–00030. This research was funded by ERC_HU, KKP_19 Programs and the PD 134195 (to Z.S.). This paper was supported by the János Bolyai Research Scholarship of the Hungarian Academy of Sciences (to Z.S.) and Doctoral Excellence Scholarship Program (DKÖP-25) (to I.S.). This work was supported by the National Research, Development, and Innovation Office (NKFIH) ADVANCED-150958 (to A.D.) and ADVANCED-153153 (to A.B.). The authors acknowledge Kinga Dóra

Kovács and Péter Joó for the initial assistance with the measurements and the technical support of the Arduino controller development. The authors acknowledge the continuous support of Béla Plósz (Plósz Mérnökiroda Kft.) in the development of the mechanical parts.

Appendix A. Supporting information

Supplementary data associated with this article can be found in the online version at doi:10.1016/j.snb.2026.141027.

Data availability

Data will be made available on request.

References

[1] E. Zamir, B. Geiger, Focal Adhesions and Related Integrin Contacts. Encyclopedia of Biological Chemistry, Elsevier, 2013, pp. 318–323, https://doi.org/10.1016/B978-0-12-378630-2.00473-4.
[2] X. Wang, et al., Mammalian cells measure the extracellular matrix area and respond through switching the adhesion state, Nat. Commun. 16 (1) (Jul. 2025) 6870, https://doi.org/10.1038/s41467-025-62153-7.
[3] K. Mandai, Y. Rikitake, M. Mori, Y. Takai, Nectins and Nectin-Like Molecules in Development and Disease. Cellular Adhesion in Development and Disease, in: Current Topics in Developmental Biology, 112, Elsevier, 2015, pp. 197–231, https://doi.org/10.1016/bs.ctdb.2014.11.019.
[4] J.T. Parsons, A.R. Horwitz, M.A. Schwartz, Cell adhesion: integrating cytoskeletal dynamics and cellular tension, Nat. Rev. Mol. Cell. Biol. 11 (9) (Sep. 2010) 633–643, https://doi.org/10.1038/nrm2957.
[5] A.V. Taubenberger, B. Baum, H.K. Matthews, The Mechanics of Mitotic Cell Rounding, Front. Cell. Dev. Biol. 8 (Aug. 2020) 687, https://doi.org/10.3389/fcell.2020.00687.
[6] C. Frantz, K.M. Stewart, V.M. Weaver, The extracellular matrix at a glance, J. Cell. Sci. 123 (24) (Dec. 2010) 4195–4200, https://doi.org/10.1242/jcs.023820.
[7] D.B. Camasão, D. Mantovani, The mechanical characterization of blood vessels and their substitutes in the continuous quest for physiological-relevant performances. A critical review, Mater. Today Bio 10 (Mar. 2021) 100106, https://doi.org/10.1016/j.mtbio.2021.100106.
[8] J. Jin, et al., The Structure and Function of the Glycocalyx and Its Connection With Blood-Brain Barrier, Front. Cell. Neurosci. 15 (Oct. 2021) 739699, https://doi.org/10.3389/fncel.2021.739699.
[9] A.W. Mulivor, H.H. Lipowsky, Role of glycocalyx in leukocyte-endothelial cell adhesion, Am. J. Physiol. -Heart Circ. Physiol. 283 (4) (Oct. 2002) H1282–H1291, https://doi.org/10.1152/ajpheart.00117.2002.
[10] S. Reitsma, D.W. Slaaf, H. Vink, M.A.M.J. van Zandvoort, M.G.A. oude Egbrink, The endothelial glycocalyx: composition, functions, and visualization, Pflüg. Arch. - Eur. J. Physiol. 454 (3) (2007) 345–359, https://doi.org/10.1007/s00424-007-0212-8. https://link.springer.com/10.1007/s00424-007-0212-8.
[11] R.T.A. Megens, S. Reitsma, P.H.M. Schiffers, R.H.P. Hilgers, J.G.R. De Mey, D. W. Slaaf, M.G.A. oude Egbrink, M.A.M.J. van Zandvoort, Two-Photon Microscopy of Vital Murine Elastic and Muscular Arteries, J. Vasc. Res. 44 (2) (2006) 87–98, https://doi.org/10.1159/000098259. https://karger.com/article/doi/10.1159/000098259.
[12] P.L. Hordijk, Recent insights into endothelial control of leukocyte extravasation, Cell. Mol. Life Sci. 73 (8) (2016) 1591–1608, https://doi.org/10.1007/s00018-016-2136-y. http://link.springer.com/10.1007/s00018-016-2136-y.
[13] N. O'Hare, K. Millican, E.E. Ebong, Unraveling neurovascular mysteries: the role of endothelial glycocalyx dysfunction in Alzheimer's disease pathogenesis, Front. Physiol. 15 (Jul. 2024) 1394725, https://doi.org/10.3389/fphys.2024.1394725.
[14] A. Suzuki, H. Tomita, H. Okada, Form follows function: The endothelial glycocalyx, Transl. Res. 247 (Sep. 2022) 158–167, https://doi.org/10.1016/j.trsl.2022.03.014.
[15] C.A. Foote, et al., Endothelial Glycocalyx, in: Y.S. Prakash (Ed.), Comprehensive Physiology, first ed., Wiley, 2022, pp. 3781–3811, https://doi.org/10.1002/cphy.c210029.
[16] T.C. Lee, V. Suresh, R.J. Clarke, Influence of endothelial glycocalyx layer microstructure upon its role as a mechanotransducer, J. Fluid. Mech. 893 (Jun. 2020) A20, https://doi.org/10.1017/jfm.2020.249.
[17] N. Kanyo, et al., Glycocalyx regulates the strength and kinetics of cancer cell adhesion revealed by biophysical models based on high resolution label-free optical data, Sci. Rep. 10 (1) (Dec. 2020) 22422, https://doi.org/10.1038/s41598-020-80033-6.
[18] P. Bełdowski, A. Mazurkiewicz, T. Topoliński, T. Małek, Hydrogen and Water Bonding between Glycosaminoglycans and Phospholipids in the Synovial Fluid: Molecular Dynamics Study, Materials 12 (13) (Jun. 2019) 2060, https://doi.org/10.3390/ma12132060.
[19] Q. Liu, et al., Engineering in vitro vascular microsystems, Microsyst. Nanoeng. 11 (1) (May 2025) 100, https://doi.org/10.1038/s41378-025-00956-w.
[20] J. Ko, et al., Microfluidic high-throughput 3D cell culture, Nat. Rev. Bioeng. 2 (6) (Apr. 2024) 453–469, https://doi.org/10.1038/s44222-024-00163-8.
[21] J. Jatzlau, et al., Fluid shear stress-modulated chromatin accessibility reveals the mechano-dependency of endothelial SMAD1/5-mediated gene transcription, iScience 26 (9) (Sep. 2023) 107405, https://doi.org/10.1016/j.isci.2023.107405.
[22] Y. Sun, B. Zhang, L. Xia, Effect of low wall shear stress on the morphology of endothelial cells and its evaluation indicators, Comput. Methods Prog. Biomed. 208 (Sep. 2021) 106082, https://doi.org/10.1016/j.cmpb.2021.106082.
[23] M. Ye, et al., Brain microvascular endothelial cells resist elongation due to curvature and shear stress, Sci. Rep. 4 (1) (Apr. 2014) 4681, https://doi.org/10.1038/srep04681.
[24] F. Melo-Fonseca, O. Carvalho, M. Gasik, G. Miranda, F.S. Silva, Mechanical stimulation devices for mechanobiology studies: a market, literature, and patents review, Bio-Des. Manuf. 6 (3) (May 2023) 340–371, https://doi.org/10.1007/s42242-023-00232-8.
[25] Y. Juste-Lanas, S. Hervas-Raluy, J.M. García-Aznar, A. González-Loyola, Fluid flow to mimic organ function in 3D *in vitro* models, APL Bioeng. 7 (3) (Sep. 2023) 031501, https://doi.org/10.1063/5.0146000.
[26] N.-W. Hu, et al., Estimation of shear stress values along endothelial tip cells past the lumen of capillary sprouts, Microvasc. Res. 142 (Jul. 2022) 104360, https://doi.org/10.1016/j.mvr.2022.104360.
[27] A.K. Wong, P. LLanos, N. Boroda, S.R. Rosenberg, S.Y. Rabbany, A Parallel-Plate Flow Chamber for Mechanical Characterization of Endothelial Cells Exposed to Laminar Shear Stress, Cell. Mol. Bioeng. 9 (1) (Mar. 2016) 127–138, https://doi.org/10.1007/s12195-015-0424-5.
[28] D. Chavarria, K.A. Georges, B.J. O'Grady, K.K. Hassan, E.S. Lippmann, Modular cone-and-plate device for mechanofluidic assays in Transwell inserts, Front. Bioeng. Biotechnol. 13 (Jan. 2025) 1494553, https://doi.org/10.3389/fbioe.2025.1494553.
[29] P. Limraksasin, et al., Shaking culture enhances chondrogenic differentiation of mouse induced pluripotent stem cell constructs, Sci. Rep. 10 (1) (Sep. 2020) 14996, https://doi.org/10.1038/s41598-020-72038-y.
[30] A. Hochstetter, Lab-on-a-Chip Technologies for the Single Cell Level: Separation, Analysis, and Diagnostics, Micromachines 11 (5) (Apr. 2020) 468, https://doi.org/10.3390/mi11050468.
[31] Y. Song, L. Ling, P. Westerhoff, C. Shang, Evanescent waves modulate energy efficiency of photocatalysis within TiO2 coated optical fibers illuminated using LEDs, Nat. Commun. 12 (1) (Jul. 2021) 4101, https://doi.org/10.1038/s41467-021-24370-8.
[32] M. Sztilkovics, et al., Single-cell adhesion force kinetics of cell populations from combined label-free optical biosensor and robotic fluidic force microscopy, Sci. Rep. 10 (1) (Jan. 2020) 61, https://doi.org/10.1038/s41598-019-56898-7.
[33] D. Yang, et al., Probing Single-Cell Adhesion Kinetics and Nanomechanical Force with Surface Plasmon Resonance Imaging, ACS Nano 19 (2) (Jan. 2025) 2651–2664, https://doi.org/10.1021/acsnano.4c14578.
[34] K.D. Kovacs, et al., Single-cell classification based on label-free high-resolution optical data of cell adhesion kinetics, Sci. Rep. 14 (1) (May 2024) 11231, https://doi.org/10.1038/s41598-024-61257-2.
[35] S.J. Altschuler, L.F. Wu, Cellular Heterogeneity: Do Differences Make a Difference? Cell 141 (4) (May 2010) 559–563, https://doi.org/10.1016/j.cell.2010.04.033.
[36] Xinglu Zhou, et al., Surface Plasmon Resonance Microscopy: From Single-Molecule Sensing to Single-Cell Imaging, Angew. Chem. 59 (5) (Jan. 2020) 1776–1785, https://doi.org/10.1002/anie.201908806.
[37] C. De Donno, et al., Population-level integration of single-cell datasets enables multi-scale analysis across samples, Nat. Methods 20 (11) (Nov. 2023) 1683–1692, https://doi.org/10.1038/s41592-023-02035-2.
[38] J. Xu, P. Zhang, Y. Chen, Surface Plasmon Resonance Biosensors: A Review of Molecular Imaging with High Spatial Resolution, Biosensors 14 (2) (Feb. 2024) 84, https://doi.org/10.3390/bios14020084.
[39] A.K. Singh, S. Mittal, M. Das, A. Saharia, M. Tiwari, Optical biosensors: a decade in review, Alex. Eng. J. 67 (Mar. 2023) 673–691, https://doi.org/10.1016/j.aej.2022.12.040.
[40] S. Alharthi, et al., Advances and Challenges in Fluorescence-Based Biosensors for Biological and Chemical Detection, ChemBioEng Rev. 12 (3) (Jun. 2025) e70006, https://doi.org/10.1002/cben.70006.
[41] G. Quaranta, G. Basset, O.J.F. Martin, B. Gallinet, Recent Advances in Resonant Waveguide Gratings, in: Laser and Photonics Reviews, 12, Wiley-VCH Verlag, Sep. 2018, https://doi.org/10.1002/lpor.201800017.
[42] Y. Fang, A.M. Ferrie, N.H. Fontaine, J. Mauro, J. Balakrishnan, Resonant Waveguide Grating Biosensor for Living Cell Sensing, Biophys. J. 91 (5) (Sep. 2006) 1925–1940, https://doi.org/10.1529/biophysj.105.077818.
[43] B. Kovacs, F.A. Kraft, Z. Szabo, Y. Nazirizadeh, M. Gerken, R. Horvath, Near cut-off wavelength operation of resonant waveguide grating biosensors, Sci. Rep. 11 (1) (Jun. 2021) 13091, https://doi.org/10.1038/s41598-021-92327-4.
[44] A.M. Ferrie, Q. Wu, O.D. Deichmann, Y. Fang, High frequency resonant waveguide grating imager for assessing drug-induced cardiotoxicity, Appl. Phys. Lett. 104 (18) (May 2014) 183702, https://doi.org/10.1063/1.4876095.
[45] A.K. Wong, P. LLanos, N. Boroda, S.R. Rosenberg, S.Y. Rabbany, A Parallel-Plate Flow Chamber for Mechanical Characterization of Endothelial Cells Exposed to Laminar Shear Stress, Cell. Mol. Bioeng. 9 (1) (2015) 127–138, https://doi.org/10.1007/s12195-015-0424-5. http://link.springer.com/10.1007/s12195-015-0424-5.
[46] J.K. Hong, L. Gao, J. Singh, T. Goh, A.M. Ruhoff, C. Neto, A. Waterhouse, Evaluating medical device and material thrombosis under flow: current and emerging technologies, Biomater. Sci. 8 (21) (2020) 5824–5845, https://doi.org/10.1039/d0bm01284j. https://pubs.rsc.org/bm/article/8/21/5824-5845/673987.
[47] H. Lu, L.Y. Koo, W.M. Wang, D.A. Lauffenburger, L.G. Griffith, K.F. Jensen, Microfluidic Shear Devices for Quantitative Analysis of Cell Adhesion, Anal. Chem.

76 (18) (2004) 5257–5264, https://doi.org/10.1021/ac049837t. https://pubs.acs.org/doi/10.1021/ac049837t.
[48] I. Sallai, Single Live Cell Assays with Label-free Optical Biosensor for the Development of Diagnostic Methods, 2025 Int. Spring Semin. Electron. Technol. (ISSE) (2025) 1–7, https://doi.org/10.1109/isse65583.2025.11121062. https://ieeexplore.ieee.org/document/11121062/.
[49] M.E. Fallon, R. Mathews, M.T. Hinds, In Vitro Flow Chamber Design for the Study of Endothelial Cell (Patho)Physiology, J. Biomech. Eng. 144 (2) (2021) 020801, https://doi.org/10.1115/1.4051765. https://asmedigitalcollection.asme.org/biomechanical/article/144/2/020801/1114550/In-Vitro-Flow-Chamber-Design-for-the-Study-of.
[50] C. Spruell, A.B. Baker, Analysis of a high-throughput cone-and-plate apparatus for the application of defined spatiotemporal flow to cultured cells, Biotechnol. Bioeng. 110 (6) (2013) 1782–1793, https://doi.org/10.1002/bit.24823. https://analyticalsciencejournals.onlinelibrary.wiley.com/doi/10.1002/bit.24823.
[51] M. Sztilkovics, T. Gerecsei, B. Peter, A. Saftics, S. Kurunczi, I. Szekacs, B. Szabo, R. Horvath, Single-cell adhesion force kinetics of cell populations from combined label-free optical biosensor and robotic fluidic force microscopy, Sci. Rep. 10 (1) (2020) 61, https://doi.org/10.1038/s41598-019-56898-7. https://www.nature.com/articles/s41598-019-56898-7.
[52] B. Beres, K.D. Kovacs, N. Kanyo, B. Peter, I. Szekacs, R. Horvath, Label-Free Single-Cell Cancer Classification from the Spatial Distribution of Adhesion Contact Kinetics, ACS Sens. 9 (11) (2024) 5815–5827, https://doi.org/10.1021/acssensors.4c01139. https://pubs.acs.org/doi/10.1021/acssensors.4c01139.
[53] K.V. Christ, K.B. Williamson, K.S. Masters, K.T. Turner, Measurement of single-cell adhesion strength using a microfluidic assay, Biomed. Microdevices 12 (3) (2010) 443–455, https://doi.org/10.1007/s10544-010-9401-x. http://link.springer.com/10.1007/s10544-010-9401-x.
[54] B.J Chung, A.M Robertson, D.G Peters, The numerical design of a parallel plate flow chamber for investigation of endothelial cell response to shear stress, Computers & Structures 81 (8-11) (2003) 535–546, https://doi.org/10.1016/s0045-7949(02)00416-9. https://linkinghub.elsevier.com/retrieve/pii/S0045794902004169.
[55] N. Orgovan, et al., Sample handling in surface sensitive chemical and biological sensing: A practical review of basic fluidics and analyte transport, Adv. Colloid Interface Sci. 211 (Sep. 2014) 1–16, https://doi.org/10.1016/j.cis.2014.03.011.
[56] V. Delprat, C. Michiels, A bi-directional dialog between vascular cells and monocytes/macrophages regulates tumor progression, Cancer Metastas. Rev. 40 (2) (Jun. 2021) 477–500, https://doi.org/10.1007/s10555-021-09958-2.
[57] B.A. Imhof, M. Aurrand-Lions, Adhesion mechanisms regulating the migration of monocytes, Nat. Rev. Immunol. 4 (6) (Jun. 2004) 432–444, https://doi.org/10.1038/nri1375.
[58] J.R. Pickett, Y. Wu, H.T. Ta, VCAM-1 as a common biomarker in inflammatory bowel disease and colorectal cancer: unveiling the dual anti-inflammatory and anti-cancer capacities of anti-VCAM-1 therapies, Cancer Metastas. Rev. 44 (2) (Mar. 2025) 40, https://doi.org/10.1007/s10555-025-10258-2.
[59] E. Nader, et al., Blood Rheology: Key Parameters, Impact on Blood Flow, Role in Sickle Cell Disease and Effects of Exercise, Front. Physiol. 10 (Oct. 2019) 1329, https://doi.org/10.3389/fphys.2019.01329.
[60] G. Tomaiuolo, S. Guido, Start-up shape dynamics of red blood cells in microcapillary flow, Microvasc. Res. 82 (1) (Jul. 2011) 35–41, https://doi.org/10.1016/j.mvr.2011.03.004.
[61] D.A. Fedosov, M. Peltomäki, G. Gompper, Deformation and dynamics of red blood cells in flow through cylindrical microchannels, Soft Matter 10 (24) (2014) 4258–4267, https://doi.org/10.1039/C4SM00248B.
[62] K.M. Saqr, et al., Physiologic blood flow is turbulent, Sci. Rep. 10 (1) (Sep. 2020) 15492, https://doi.org/10.1038/s41598-020-72309-8.
[63] H.L. Zhou, X.Z. Jiang, Y. Ventikos, Role of blood flow in endothelial functionality: a review, Front. Cell. Dev. Biol. 11 (Oct. 2023) 1259280, https://doi.org/10.3389/fcell.2023.1259280.
[64] C. Luk, N.J. Haywood, K.I. Bridge, M.T. Kearney, Paracrine Role of the Endothelium in Metabolic Homeostasis in Health and Nutrient Excess, Front. Cardiovasc. Med. 9 (Apr. 2022) 882923, https://doi.org/10.3389/fcvm.2022.882923.
[65] S. Liu, J. Cai, Z. Chen, Vascular mechanical forces and vascular diseases (Sep), J. Adv. Res. (2025) S2090123225006964, https://doi.org/10.1016/j.jare.2025.09.013.
[66] D.G. Harrison, J. Widder, I. Grumbach, W. Chen, M. Weber, C. Searles, Endothelial mechanotransduction, nitric oxide and vascular inflammation, J. Intern. Med. 259 (4) (Apr. 2006) 351–363, https://doi.org/10.1111/j.1365-2796.2006.01621.x.
[67] B.R. Kwak, et al., Biomechanical factors in atherosclerosis: mechanisms and clinical implications, Eur. Heart J. 35 (43) (Nov. 2014) 3013–3020, https://doi.org/10.1093/eurheartj/ehu353.
[68] C. Collins, "Understanding PECAM-1-mediated mechanotransduction: from the protein to the vessel," University of North Carolina at Chapel Hill. doi: 10.17615/KSQR-HE98.
[69] L. Ramage, Integrins and extracellular matrix in mechanotransduction, Cell. Health Cytoskelet. (Dec. 2011) 1, https://doi.org/10.2147/CHC.S21829.
[70] X. Kong, A. Kapustka, B. Sullivan, G.J. Schwarz, D.E. Leckband, Extracellular matrix regulates force transduction at VE-cadherin junctions, Mol. Biol. Cell. 33 (11) (Sep. 2022) ar95, https://doi.org/10.1091/mbc.E22-03-0075.
[71] S. Altenhöfer, et al., The NOX toolbox: validating the role of NADPH oxidases in physiology and disease, Cell. Mol. Life Sci. 69 (14) (Jul. 2012) 2327–2343, https://doi.org/10.1007/s00018-012-1010-9.
[72] R.S. Frey, M. Ushio–Fukai, A.B. Malik, NADPH oxidase-dependent signaling in endothelial cells: role in physiology and pathophysiology, Antioxid. Redox Signal. 11 (4) (Apr. 2009) 791–810, https://doi.org/10.1089/ars.2008.2220.
[73] H. Harjunpää, M. Llort Asens, C. Guenther, S.C. Fagerholm, Cell Adhesion Molecules and Their Roles and Regulation in the Immune and Tumor Microenvironment, Front. Immunol. 10 (May 2019) 1078, https://doi.org/10.3389/fimmu.2019.01078.
[74] B.M. Gumbiner, Cell Adhesion: The Molecular Basis of Tissue Architecture and Morphogenesis, Cell 84 (3) (Feb. 1996) 345–357, https://doi.org/10.1016/S0092-8674(00)81279-9.
[75] R. Kumari, et al., Focal adhesions contain three specialized actin nanoscale layers, Nat. Commun. 15 (1) (Mar. 2024) 2547, https://doi.org/10.1038/s41467-024-46868-7.
[76] G.F. Weber, M.A. Bjerke, D.W. DeSimone, Integrins and cadherins join forces to form adhesive networks, J. Cell. Sci. 124 (8) (Apr. 2011) 1183–1193, https://doi.org/10.1242/jcs.064618.
[77] Z. Szekanecz, A.E. Koch, Vascular endothelium and immune responses: implications for inflammation and angiogenesis, Rheum. Dis. Clin. N. Am. 30 (1) (Feb. 2004) 97–114, https://doi.org/10.1016/S0889-857X(03)00116-9.
[78] K. Ley, The role of selectins in inflammation and disease, Trends Mol. Med. 9 (6) (Jun. 2003) 263–268, https://doi.org/10.1016/S1471-4914(03)00071-6.
[79] D. Ribatti, R. Tamma, T. Annese, Epithelial-Mesenchymal Transition in Cancer: A Historical Overview, Transl. Oncol. 13 (6) (Jun. 2020) 100773, https://doi.org/10.1016/j.tranon.2020.100773.
[80] N. Orgovan, B. Peter, S. Bősze, J.J. Ramsden, B. Szabó, R. Horvath, Dependence of cancer cell adhesion kinetics on integrin ligand surface density measured by a high-throughput label-free resonant waveguide grating biosensor, Sci. Rep. 4 (1) (Feb. 2014) 4034, https://doi.org/10.1038/srep04034.
[81] F. Wang, Y. Li, Y. Shen, A. Wang, S. Wang, T. Xie, The Functions and Applications of RGD in Tumor Therapy and Tissue Engineering, Int. J. Mol. Sci. 14 (7) (Jun. 2013) 13447–13462, https://doi.org/10.3390/ijms140713447.
[82] S.E. D'Souza, M.H. Ginsberg, E.F. Plow, Arginyl-glycyl-aspartic acid (RGD): a cell adhesion motif, Trends Biochem. Sci. 16 (Jan. 1991) 246–250, https://doi.org/10.1016/0968-0004(91)90096-E.
[83] A.D. Rosen, Mechanism of Action of Moderate-Intensity Static Magnetic Fields on Biological Systems, Cell Biochem. Biophys. 39 (2) (2003) 163–174, https://doi.org/10.1385/cbb:39:2:163. http://link.springer.com/10.1385/CBB:39:2:163.
[84] S. Ghodbane, A. Lahbib, M. Sakly, H. Abdelmelek, Bioeffects of Static Magnetic Fields: Oxidative Stress, Genotoxic Effects, and Cancer Studies, Biomed. Res. Int. 2013 (2013) 1–12, https://doi.org/10.1155/2013/602987. http://www.hindawi.com/journals/bmri/2013/602987/.
[85] L. Zhang, X. Ji, X. Yang, X. Zhang, Cell type- and density-dependent effect of 1 T static magnetic field on cell proliferation, Oncotarget 8 (8) (2017) 13126–13141, https://doi.org/10.18632/oncotarget.14480. https://www.oncotarget.com/lookup/doi/10.18632/oncotarget.14480. (Accessed 4 January 2017).
[86] H. Gurhan, R. Bruzon, S. Kandala, B. Greenebaum, F. Barnes, Effects Induced by a Weak Static Magnetic Field of Different Intensities on HT-1080 Fibrosarcoma Cells, Bioelectromagnetics 42 (3) (2021) 212–223, https://doi.org/10.1002/bem.22332. https://onlinelibrary.wiley.com/doi/10.1002/bem.22332. (Accessed 18 March 2021).
[87] T.-C. Wang, et al., Genetic variation drives cancer cell adaptation to ECM stiffness, Proc. Natl. Acad. Sci. 121 (39) (Sep. 2024) e2403062121, https://doi.org/10.1073/pnas.2403062121.
[88] Y. Xin, et al., Circulating tumor cells with metastasis-initiating competence survive fluid shear stress during hematogenous dissemination through CXCR4-PI3K/AKT signaling, Cancer Lett. 590 (May 2024) 216870, https://doi.org/10.1016/j.canlet.2024.216870.
[89] R. Ungai-Salánki, et al., Single-cell adhesion strength and contact density drops in the M phase of cancer cells, Sci. Rep. 11 (1) (Sep. 2021) 18500, https://doi.org/10.1038/s41598-021-97734-1.
[90] C. Yang, M.W. Tibbitt, L. Basta, K.S. Anseth, Mechanical memory and dosing influence stem cell fate, Nat. Mater. 13 (6) (Jun. 2014) 645–652, https://doi.org/10.1038/nmat3889.
[91] C.X. Li, et al., MicroRNA-21 preserves the fibrotic mechanical memory of mesenchymal stem cells, Nat. Mater. 16 (3) (Mar. 2017) 379–389, https://doi.org/10.1038/nmat4780.
[92] A.R. Killaars, J.C. Grim, C.J. Walker, E.A. Hushka, T.E. Brown, K.S. Anseth, Extended Exposure to Stiff Microenvironments Leads to Persistent Chromatin Remodeling in Human Mesenchymal Stem Cells, Adv. Sci. 6 (3) (Feb. 2019) 1801483, https://doi.org/10.1002/advs.201801483.
[93] J. Dai, et al., Tracing back primed resistance in cancer via sister cells, Nat. Commun. 15 (1) (Feb. 2024) 1158, https://doi.org/10.1038/s41467-024-45478-7.
[94] B.A. Biddy, et al., Single-cell mapping of lineage and identity in direct reprogramming, Nature 564 (7735) (Dec. 2018) 219–224, https://doi.org/10.1038/s41586-018-0744-4.